



OUTDOOR FESTIVAL LICENSE APPLICATION

1001 EAST 9TH STREET, BUILDING A

P.O. BOX 11130

RENO, NEVADA 89520-0027

(775) 328-3733

www.washoecounty.us

OUTDOOR FESTIVAL LICENSE GENERAL PROCEDURES

Definition: "Outdoor festival" means an assembly of 1,000 or more persons on any 1 day of the event gathered together for any purpose, at any location, other than a permanent building or permanent installation that has been constructed for and will accommodate the number of persons gathered therein

1. **APPLICATION.** Complete the form in ink. This application is for events with attendance over 1,000 persons (spectators and participants) on any one day of the event. There is a \$1,000.00 nonrefundable application fee. Applications will be returned if the application fee is not included. Three paper copies of the application plus an electronic pdf file (memory stick or DVD) of the application must be turned in at least **90 days** before the event. The application must include all required forms.
2. **APPLICATION DEADLINE.** All applications must be submitted at least **90 days** in advance of the event.
3. **LICENSING REQUIREMENTS.** An outdoor festival license is required on any public or private lands in the unincorporated area of Washoe County except for lands managed by the Washoe County Regional Parks and Open Space; and, state, trust, tribal, and federal lands. All events must meet land use/regulatory zone requirements before the license will be issued. For information on land use/regulatory zone requirements, call (775) 328-6100 with the parcel number(s) of the event.
4. **BONDS.** The outdoor festival license will not be issued until the applicant has agreed to hold harmless, and has submitted evidence of sufficient insurance to indemnify, the County of Washoe, and their employees, agents and contractors for any and all liability for damages, injury, loss or expense caused or occasioned by reason of an act, or failure to act on the part of the applicant, the sponsoring organization, their agents and employees throughout the event. Additional bonds or letters of credit may be required.
5. **FEES.** The license fee for an outdoor festival is \$350.00 per day plus any booth fees if applicable. If the event is a carnival, circus or tent show the daily license fee is \$300, to a maximum amount of \$4,200, plus booth fees if applicable.

BOOTH FEES			
1-4 booths	\$ 25	50-59 booths	\$ 30
5-9 booths	\$ 50	60-69 booths	\$ 350
10-19 booths	\$ 100	70-79 booths	\$ 400
20-29 booths	\$ 150	80-89 booths	\$ 45
30-39 booths	\$ 200	90-100 booths	\$ 500
40-49 booths	\$ 250	More than 100 booths	\$ 500 plus \$5 for each booth in excess of 100

6. **INVESTIGATION.** The Sheriff's Office shall conduct a criminal history inquiry of the applicants (to include partners and corporate officers). Fingerprint impressions may be taken and submitted to the Nevada Central Repository for criminal history records and the Federal Bureau of Investigation. Fingerprint impressions will be taken after the application is turned in and deemed complete. A local police records check may be substituted for the criminal history inquiry for applicants with prior approved outdoor festival license(s) for the same type of event.
7. **CONDITIONS.** All pre-event conditions imposed by the Washoe County Board of County Commissioners (BCC) for the outdoor festival license must be met before the license will be issued.
8. **APPROVALS AND AGENCY SIGN-OFFS.** The application will be reviewed by the appropriate agencies, to include Building and Safety, the District Attorney's Office, Engineering, Health District, fire agency, the Sheriff's Office, and other agencies as appropriate. The application will be approved by the BCC at a public hearing.
9. **ISSUANCE OF LICENSE.** The outdoor festival license will be issued after all fees have been paid and all required pre-event conditions are met. The outdoor festival license must be displayed prominently at the event and must be available for inspection. This license is valid only for the event authorized and not for any other event.

OUTDOOR FESTIVAL LICENSE

Materials required for submittal

_____ Fees – check(s) made payable to “Washoe County”

Application fee

_____ \$1,000 non-refundable application fee

Daily fee(s)

_____ \$350 daily fee plus appropriate booth fees

Carnival, circus or tent show fees

_____ \$100 daily fee (maximum of \$1,400) plus appropriate booth fees

_____ Three packets plus an electronic pdf file (memory stick or DVD). Each packet shall include the completed application and event plan. The event plan must include:

_____ Site plan showing the arrangement of all facilities; including ingress, egress, parking and camping; and,

Detailed explanations for:

_____ Security and fire protection

_____ Water supply and facilities

_____ Sanitation facilities

_____ Medical facilities and services

_____ Vehicle parking

_____ Vehicle access and on-site traffic control

_____ Communication system

_____ Illuminating the premises (if applicable)

_____ Camping (if applicable)

_____ Cleanup and rubbish removal plan and cost estimates to return the event site to its pre-event condition

_____ Certified copies of articles of incorporation filed in Nevada (if applicable)

_____ Copy of partnership papers (if applicable)

_____ Insurer Information and copy of insurance policy specific to event (copy must be furnished prior to the issuance of the license), History of similar events, and Vendor list

Submission Materials (continued)

- _____ Property ownership affidavit and permission to conduct event signed by each property owner(s) and notarized (separate form for each property owner)
- _____ Statement of Assets
- _____ Statement of Liabilities
- _____ Personal history of all applicants (to include corporate officers and partners)
- _____ Names and addresses of any person contributing, investing or having an expected financial interest greater than \$500 in producing the event
- _____ Names and addresses of any person expected to provide, for consideration, services or activities ancillary to or in conjunction with the event
- _____ Release of claims and authorization to release information signed by each applicant (to include corporate officers and partners) and notarized
- _____ Insurance, Hold Harmless & Indemnification Requirements signed by applicant
- _____ Waiver and Consent to Extend Mandated Public Hearing Date signed by applicant

OUTDOOR FESTIVAL LICENSE APPLICATION

(Requires a non-refundable \$1,000 application fee)

3/16/18

Application date: _____

Applicant Information

Applicant's name: Happy Fun Events LLC

Mailing address: 2764 W 479 N Provo UT 84601

Street or PO Box City State Zip code

Phone: 801-318-0679 (Business) 801-400-4842 (Home) 801-400-4842 (Cell)

All applicants, to include corporate officers or partners must complete a personal history form

Is the applicant a(n): ☒ Corporation ☐ Partnership ☐ Individual

If a corporation or a partnership, list corporate officers or partners:

Name	Address	Title
Martha Hunn	207 S Sequoia Circle Alpine, UT 84004	Director

Event Information

Name of Event: The Lantern Fest

Date(s) of Event: 5/26/18 Hours of operation: 15:00 to 22:00

Location of Event: Wild West Motorsports Park 12005 East I-80, Sparks, NV 89434

Assessor Parcel Number(s): Parcel # 084-060-13

Description of Event: The Lantern Fest is a family friendly out door concert and festival that culminates in a 20 minute sky lantern launch. For further description please see appendix A.

Name of the designated event representative who will be on-site during the event and who has authority to bind the applicant: Eric Brooks

Will an admission fee be charged for your event? ☒ Yes ☐ No

If yes, amount and type of fee(s): \$50/Adult \$10/Child

When will fee be collected? ☒ Pre-sales ☐ At entrance

Approximate number of participants and other persons: 9,000

Approximate number of customers and spectators: Same as above.

Approximate maximum number of persons on any one day of the event: 9,000

Will food and/or beverages be served? ☒ Yes ☐ No

(all food and beverage vendors must have the appropriate Washoe County Health District permits)

Will alcoholic beverages be served? ☒ Yes ☐ No

(all intoxicating liquor vendors must be individually licensed with Washoe County Business License)

Will there be live music? ☒ Yes ☐ No

OUTDOOR FESTIVAL LICENSE

INSURER INFORMATION

(see Insurance, Hold Harmless & Indemnification Requirements)

Western State Insurance Company

See appendix

Name of Insurer: _____ Policy number: K

Attach copy of insurance policy specific to event (must be furnished prior to the issuance of the license)

Address of Insurer:	87 East Center Street	Spanish Fork	UT	84660
	Street	City	State	Zip code

Limits of liability: 6,000,000/Occurrence 6,000,000/Aggregate

HISTORY OF SIMILAR EVENTS

(attach additional sheets if needed)

Describe the history of all similar events conducted, operated or promoted by the applicant. Include, at a minimum, event names, types, dates, locations, permits or licenses issued.

We have done this exact even over 150 times, in at least 30 different locations, in the last three year. We have a global footprint and have

done quite a few events in the intermountain west. The following are three venues that have hosted events similiar in size to the event at WildWest Motorsports Park.

-Grantsville, UT. Two events a year since 2015. Mayor Brent Marshall. Phone: (435) 884-3411. Special Event Permit.

-Long Pond, PA. Two events a year since 2015. Nick Igdalsky. 570-646-2300. Special Event Permit.

-Post Falls, ID. One event a year since 2014. Dean Boever. 208-773-0100. Special Events Permit.

VENDOR LIST

(attach additional sheets if needed)

Name of Vendor

Type of product

N/A

N/A

OUTDOOR FESTIVAL LICENSE
AFFIDAVIT OF PROPERTY OWNERSHIP
and/or PERMISSION TO CONDUCT EVENT

STATE OF NEVADA)

COUNTY OF WASHOE)

ss:

I, Ronald J. Bath, Managing Partner for Lockwood Investments being duly sworn, depose, and say that I am an owner* of property involved in this outdoor festival and I do hereby:

(check appropriate box)

☐ Affirm that I am an applicant for the below named proposed outdoor festival and also own the property or properties on which the event will be conducted

OR

☒ Affirm that I give permission to the applicants for the below named proposed outdoor festival to conduct the event on the following property or properties which I own:

Assessor Parcel Number(s): 084-060-13

Proposed Outdoor Festival: Lantern Festival

Signed R. J. Bath
Ronald J. Bath

Subscribed and sworn to before me this 16th day of March, 2018

[Signature]
Notary Public in and for said county and state

My commission expires: January 13th, 2020

*Owner refers to the following. Please mark the appropriate box.

- ☒ OWNER/JOINT OWNER
☐ CORPORATE OFFICER/PARTNER
☐ POWER OF ATTORNEY (Provide copy of Power of Attorney)
☐ AGENT (Notarized letter from property owner giving legal authority to agent)
☐ LETTER FROM GOVERNMENT AGENCY WITH STEWARDSHIP

**OUTDOOR FESTIVAL LICENSE
STATEMENT OF ASSETS**

As of March 16, 2018

(Describe fully and indicate assets pledged)
(If additional space is required, attached supporting pages or documents)

Current Assets

Cash on hand	\$ <u>.00</u>
Cash in safe deposit box	\$ <u>.00</u>
Cash in <u>Wells Fargo</u> <u>1095 E 2100 S, Salt Lake City, UT 84106</u>	\$ <u>123,000.00</u>
Cash in <u>NA</u>	\$ <u>.00</u>
Accounts and notes receivable (describe nature of receivable and when due)	\$ <u>435,000</u>
Registration. Due by May 14, 2018	
Other current assets	
N/A	

Investments

Stocks, Bonds, etc (Market value) (If close held corporation, furnish current balance sheet)	
N/A	
Investments, other than stocks and bonds	
N/A	

Fixed assets

Real estate (Give location, description and fair value of each parcel)	
N/A	

Other assets

Automobiles and other personal property	\$ <u>75,000</u>
Hard assets associated with the event. Vehicles etc.	
Total Assets	\$ <u>633,000.00</u>

Spencer Humiston

Print Name

Signature

3/16/18

Date

**OUTDOOR FESTIVAL LICENSE
STATEMENT OF LIABILITIES**

As of March 16, 2018

(Describe fully, indicate secured liabilities)

(If additional space is required, attached supporting pages or documents)

Current liabilities

Notes payable _____ \$ 0

Name, Bank and Branch

Due _____ How secured _____

Notes payable _____ \$ 0

Name, Bank and Branch

Due _____ How secured _____

Notes payable _____ \$ 0

Name, Bank and Branch

Due _____ How secured _____

Notes payable _____ \$ 0

Name, Bank and Branch

Due _____ How secured _____

Other notes payable (indicate name, address and how secured)

_____ \$ 0

_____ \$ 0

Accounts payable \$ 0

Liability for Federal Income Tax (delinquent) \$ 0

Provision for current year's Federal Income Tax \$ 0

Provisions for other current taxes \$ 0

Liability for other delinquent taxes \$ 0

Mortgages payable (List each mortgage separately, how secured, and monthly payments due thereon)

_____ \$ 0

_____ \$ 0

Other liabilities

_____ \$ 0

_____ \$ 0

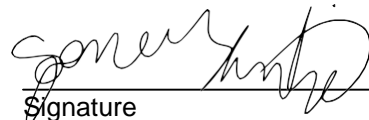
_____ \$ 0

Total Liabilities \$ 0

Contingent liabilities (describe)

Spencer Humiston

Print Name


Signature

3/16/18

Date

OUTDOOR FESTIVAL LICENSE

CONTRIBUTORS OR INVESTORS LIST

(List the names and addresses of any person contributing, investing or having an expected financial interest greater than \$500 in producing the event)
(attach additional sheets if needed)

Name
N/A

Address
N/A

ANCILLARY SERVICES OR ACTIVITIES LIST

(List the names and addresses of any person expected to provide, for consideration, services or activities ancillary to or in conjunction with the event)
(attach additional sheets if needed)

Name
N/A

Address
N/A

OUTDOOR FESTIVAL LICENSE RELEASE OF CLAIMS

(complete a separate form for each applicant, to include corporate officers and partners)

The undersigned has filed with Washoe County Business License an application for outdoor festival license. In consideration of the assurance by the Washoe County Board of County Commissioners that no vote on said application will be taken except after a deliberate, intensive and thorough investigation of the undersigned, including but not limited to a criminal history inquiry, associates and finances, the undersigned does for himself, his heirs, executors, administrators, successors and assigns, hereby release, remise and forever discharge the County of Washoe, Washoe County Board of County Commissioners, Washoe County Sheriff's Office, and Washoe County Business License from any and all manner of actions, causes of action, suits, debts, judgments, executions, claims, and demands whatsoever, known or unknown, in law or equity, which the undersigned ever had, now has or may have, or claim to have against any or all of said entities or individuals arising out of or by reason of the processing or investigation of or other action relating to the undersigned application.

AUTHORIZATION TO RELEASE INFORMATION

As an applicant for an outdoor festival license with Washoe County Business License, I am required to furnish information for use in determining my qualifications. In this connection, I authorize release of any and all information of a confidential or privileged nature.

I hereby release you, your organization and others from liability or damage, which may result from furnishing the information requested. This release will expire 180 days after the date signed.

I, the undersigned, having read this release and authorization and understanding all its terms, execute the release and authorization voluntarily and with full knowledge of its significance.

IN WITNESS WHEREOF, I have executed this release/authorization at _____ on the _____ day of _____, 20_____.

Printed name of applicant

Signature of applicant

Subscribed and sworn to before me this _____ day of _____, 20_____

Notary Public in and for said county and state

My commission expires: _____

OUTDOOR FESTIVAL LICENSE

INSURANCE, HOLD HARMLESS AND INDEMNIFICATION REQUIREMENTS

Pursuant to Washoe County Code section 25.303, any applicant for a Washoe County outdoor festival license must ensure the following requirements are met to the satisfaction of the Washoe County Risk Management Division before the outdoor business license may be issued.

INDEMNIFICATION & HOLD HARMLESS

As respects acts, errors or omissions relating to the event, APPLICANT agrees to indemnify and hold harmless the COUNTY, its officers, agents, employees, and volunteers from and against any and all claims, demands, defense costs, liability or consequential damages of any kind or nature arising directly or indirectly out of the event or any activity leading up to, during, or following the event, excepting those which arise out of the sole negligence of the COUNTY.

APPLICANT further agrees to defend the COUNTY and assume all costs, expenses and liabilities of any nature to which the COUNTY may be subjected as a result of any claim, demand, action or cause of action arising out of the negligent acts, errors or omissions of the APPLICANT or its agents concerning the event.

INSURANCE REQUIREMENTS

The COUNTY requires that the APPLICANT purchase General Liability Insurance as described below against claims for injuries to persons or damages to property which may arise from or in connection with the event by the APPLICANT, its agents, representatives, or employees. The cost of all such insurance shall be borne by the APPLICANT.

APPLICANT shall maintain coverage and limits no less than \$1,000,000 combined single limit per occurrence for bodily injury, personal injury and property damage. If Commercial General Liability Insurance or other form with a general aggregate limit is used, the general aggregate limit shall be increased to equal twice the required occurrence limit, to apply separately to this event.

Any deductibles or self-insured retentions must be declared to and approved by the COUNTY Risk Management Division prior to the event. The COUNTY reserves the right to request additional documentation, financial or otherwise prior to giving its approval of the deductibles and self-insured retention and prior to issuing the license. The COUNTY Risk Manager prior to the change taking effect must approve any changes to the deductibles or self-insured retentions.

APPLICANT shall provide the COUNTY with a certificate of insurance that identifies the COUNTY, its officers, agents, employees and volunteers as additional insured's.

NOTE: A certificate of insurance complying with the provisions stated above is not required with the outdoor festival license application, but must be furnished prior to the issuance of the license.

I hereby agree to the all of the provisions stated above:

The Lantern Fest

5/26/18

Name of Event

Date(s) of Event

Spencer Humiston



Applicant's name (printed)

Applicant's signature

Date: 3/16/18

OUTDOOR FESTIVAL LICENSE

Memorandum for:

Office of the Washoe County Clerk
1001 East 9th St. Bldg A – 1st Floor
Reno, Nevada

Subject: Waiver and Consent to Extend Mandated Public Hearing Date before the
Washoe County Commission for Outdoor Festival License Application

Nevada Revised Statutes (NRS) 244.3544 and Washoe County Code (WCC) section 25.277 require the County Clerk to set a public hearing date before the Washoe County Board of County Commissioners for an outdoor festival license application no later than 30 days after the application is deemed complete and application fees are received. These two regulations also require that specific County agencies review the application and provide written reports to the Board of County Commissioners, to include recommendations on the license and conditions if appropriate.

The mandated review by County agencies on the license application is of utmost importance to both Washoe County and the applicant, to ensure that the festival is conducted in a manner that protects public health, safety and welfare. To this end, the undersigned license applicant agrees to waive the 30 day public hearing time limit imposed by NRS 244.3544 and WCC section 25.277.

As the undersigned license applicant, I agree to extend the required Board of County Commissioners public hearing date to occur no more than 90 days after the application is deemed complete and application fees are received, and no less than 15 days prior to the date when the outdoor festival is proposed to commence.

Attest:

License Applicant



Signature

3/16/18

Date

Spencer Humiston

Printed Name

The Lantern Fest

Representing

LLC
Certificate of Organization
OF
Happy Fun Events, LLC

The undersigned person(s) do hereby adopt the following Certificate of Organization for the purpose of forming a Utah Limited Liability Company.

Article I

The name of the limited liability company is to be Happy Fun Events, LLC

Article II

The purpose or purposes for which the company is organized is to engage in:
Event planning

The Company shall further have unlimited power to engage in or to perform any and all lawful acts pertaining to the management of any lawful business as well as to engage in and to do any lawful act concerning any and all lawful business for which a Limited Liability Company may be organized under the Utah Limited Liability Company Act and any amendments thereto.

Article III

The Company shall continuously maintain an agent in the State of Utah for service of process who is an individual residing in said state. The name and address of the initial registered agent shall be:

(Registered Agent Name & Address)
Martha Porter Hunn
207 Sequoia Circle
Apline, UT, 84004



Article IV

Name, Street address & Signature of all members/managers

Manager #1
Martha Porter Hunn
207 Sequoia Circle
Apline, UT 84004
Martha Porter Hunn
Signature

DATED 28 June, 2016.

Article V

Management statement

This limited liability company will be managed by its Managers

Article VI

Records required to be kept at the principal office include, but are not limited to the following:

Article VI.1

A current list in alphabetical order of the full name and address of each member and each manager.

Article VI.2

A copy of the stamped certificate of Organization and all certificates of amendments thereto.

Article VI.3

Copies of all tax returns and financial statements of the company for the three most recent years.

Article VI.4

A copy of the company's operating agreement and minutes of each meeting of members.

Article VII

The street address of the principal place of business is:

207 Sequoia Circle
Apline, UT 84004

Article VIII

The duration of the company shall be Perpetual

Under GRAMA {63-2-201}, all registration information maintained by the Division is classified as public record. For confidentiality purposes, the business entity physical address may be provided rather than the residential or private address of any individual affiliated with the entity.

APPENDIX A through K

Appendix A

MISSION STATEMENT:

To illuminate the human spirit—bringing together family and friends through the joy of spectacle.

THE EVENT:

Historically lanterns were used to symbolize good fortune, request favorable weather, and to celebrate the life of a loved one. Regardless of the motivation for lighting a lantern, families and friends can dance to the music, roast marshmallows for their s'mores, munch on snacks provided by local vendors, and of course, send off their lanterns and watch them float away in a spectacular release.

CHARITY:

Part of the proceeds from The Lantern Fest will be donated to a local charity that partners with us in the event.

PARTICIPANTS:

We anticipate 8,000 participants to attend this family friendly event. It's an all ages event, but only those 16 and older are allowed to participate in the lighting of the lanterns; all others can attend as spectators.

HOW IT'S DONE:

Marketing:

We market the event via our website, social media, and other forms of advertising for 2-3 months prior to the event.

Registration:

Participants may register on our website at www.thelanternfest.com or they may purchase tickets the day of the Event (if the event is not sold out). Pricing is based on the time of purchase and varies. Sometimes third party vendors (i.e. Groupon or Living Social) may be used.

- On Site Check-in opens at 3pm and continues until the launch.

PRE-LAUNCH PREPARATION:

- Participants are assigned to a specific area, where they can roast marshmallows, enjoy on site festivities, and chat with family and friends.
- Launch times are determined by sunset and weather conditions, but lanterns are usually lit and set afloat between the hours of 6:30pm-9pm.
- The launch lasts about 20 minutes and then concludes. The Lantern Fest begins to quickly clean up the lanterns and the venue.

ENTERTAINMENT:

Food from local vendors or concessions

- Live Music or DJ
 - Lantern decorating
 - Making S'mores
 - Face painting
 - Balloon making
 - Kids Favorite Character Impersonators
 - Creating memories
 - Kids Entertainment (including competitions)
-
- Food from local vendors or concessions
 - Live Music or DJ
 - Lantern decorating
 - Making S'mores
 - Face painting
 - Balloon making
 - Kids Favorite Character Impersonators
 - Creating memories
 - Kids Entertainment (including competitions)

Appendix B

Security and Fire Protection

At a minimum we will take the following precautions for all of our event. If the local authority requests additional steps be taken, we will also implement that guidance into our plan.

- The Lantern Fest will coordinate all of it's safety and fire procedures with jurisdictional authority and follow the guidance and expertise of city, county, and municipality officials in the weeks and days preceding the event.
- Work closely with the jurisdictional authority to ensure all proper permitting and regulations requirements are correctly fulfilled.
- Coordinate with Wildwest Motorsports Park to ensure their standard fire/safety policies and procedures are in place and functioning.
- Coordinate with jurisdictional authority 3 days before the event, and then again on the day of the event, to ensure there are no burn bans, unforeseen fire hazards, or adverse weather conditions.
- Request final authorization from jurisdictional authority before the actual lantern launch.
- Once final authorization is received The Lantern Fest will launch 2-3 test lanterns to approximate where the entirety of the lanterns. The Lantern Fest will then post fire suppression units in that area.
- Ensure that all participants and spectators within the venue are accounted for and have signed waivers.
- Provide instruction to participants regarding the proper way to light and release lanterns. We send the participants an instructional video upon registration, and then provide several additional instructional opportunities during the event.
- Ensure that all sources of flames at the event are properly and safely secured, protected, and accounted for by volunteers during the entirety of the event.
- Per the advice of fire authorities, no participants under the age of 16 are allowed to light or handle the lit lanterns. Participants under 16 years of age wear a separate wristband helping staff identify their age.
- Each event will be staffed with no less than the number of volunteers/personnel suggested by the local fire authority, but under no circumstances will The Lantern Fest have less than 40 volunteers and fulltime staff supervising the lantern launch.

- During the entirety of the event, each volunteer will be in the possession of an individual fire suppression device. A total of 100 fire suppression devices will be easily accessible to participants and volunteers.
- Use exclusively sourced, 100% biodegradable, flame retardant lanterns with a limited burn time of 4 to 5 minutes.
- Each volunteer will be responsible for a pre-assigned segment of the launch area and will have access to a dedicated walkie talkie in the event they need to call for assistance.
- Licensed paramedics will be on call at each event. They will have a privacy tent and ambulance on site.
- If required or suggested by jurisdictional authority, a licensed pyrotechnic expert will be at the event.
- The Lantern Fest will ensure that a proper number of safety/security professional will be at each event.
- If requested by jurisdictional authority, a number of local fire professionals will be in attendance with either a brush or water truck. They will also be in possession of their own fire suppression units. (The Lantern Fest provides discounted/free attendance for local fire fighters).
- If required by local fire professionals The Lantern Fest will hire private fire suppression units to patrol the area where lanterns are landing UTVs.
- Entrances and Exits (including Emergency Exit) signs shall be posted.
- Every participant will sign a waiver and agree to all previously stated safety precautions.
- The Lantern Fest carries, at a minimum, a one million dollar per event insurance policy.
- The Lantern Fest receives a Letter of No Objection from the FAA for every scheduled event.

Recovery Procedures

Our recovery plan for this event consists of three separate phases: immediately after the lantern launch, two to three hours post launch, and the morning after the lantern launch.

DURING AND IMMEDIATELY AFTER THE LAUNCH

We will station a lantern spotter somewhere in the venue where they will have good visibility of the lantern landing area. As soon as the lanterns are launched, will send a truck with at least 3 individuals equipped with fire extinguishers to the area where the lanterns are beginning to land. They will be equipped with walkie talkies and will remain

in that general area for the duration of the launch and will stay there for at least an hour after the launch.

TWO TO THREE HOURS POST LAUNCH

The crew will be at the speedway until at least midnight. From 9 pm to Midnight we will keep a spotter stationed while we clean up the track and surrounding area. Before returning to the hotel at midnight, we will send a number of my crew through the lantern landing area to ensure none of the lanterns are still warm.

MORNING AFTER THE LAUNCH

We will arrive back at the speedway at 6:30 am with a crew of about 50 volunteers. Over the next 5 hours we will scour the lantern landing area and pick up all the lanterns that were released the evening before.

Appendix C

Water Supply and Facilities

There is no potable water at The WildWest Motorsports Park. The Lantern Fest will follow the guidance of Washoe County Health department, and all other involved department's, guidance regarding requirements for potable water. The Lantern Fest will meet, at least, the minimum requirements from those departments.

Appendix D

Sanitation Facilities

The Lantern Fest will coordinate with appropriate departments to ensure that required sanitation facilities, toilets, and hand washing are provided. At a minimum The Lantern Fest will provide 88 portable toilets (6 ADA toilets),, 4 handwashing stations, and any other required sanitation facilities. The Lantern Fest will also keep The WildWest Motorsports Park's sanitation facilities open and stocked during the duration of the event.

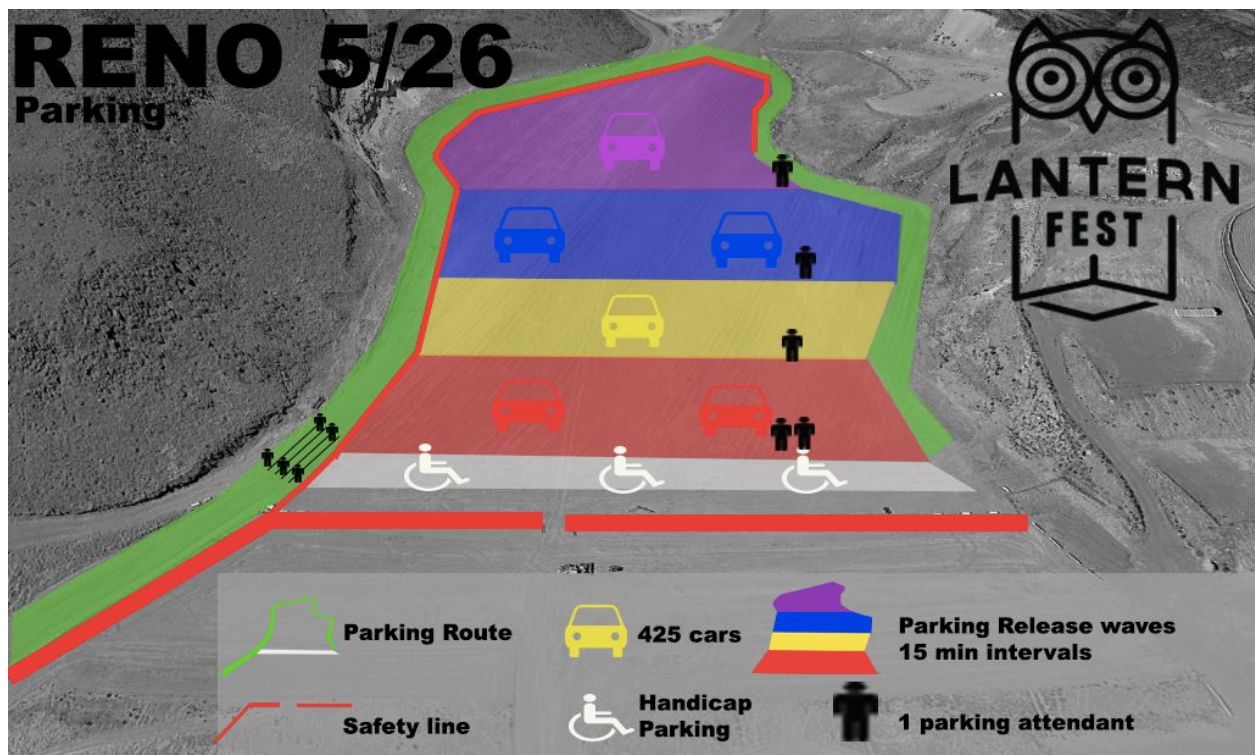
Appendix E

Medical facilities and services

Please see Appendix D. Licensed paramedics will be on call at each event. They will have a privacy tent and ambulance on site. We will also follow requirements already established by the county for Wild West Motorsports Park. Furthermore, The Lantern Fest will follow any and all guidance provided by appropriate county agencies.

Appendix F

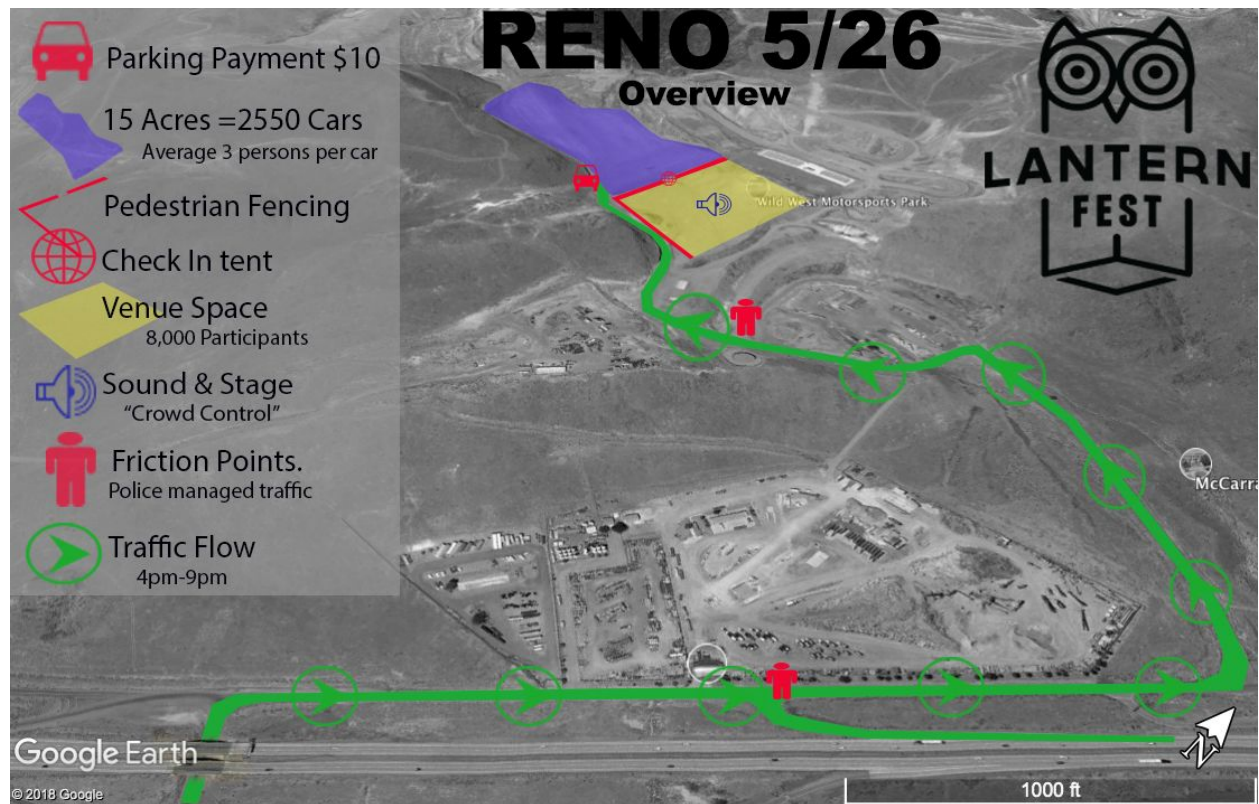
Vehicle Parking



The Lantern Fest releases parked cars in waves in 15 minute intervals, thereby allowing there to be less pressure on egress exits. The Lantern Fest will work closely with the venue and jurisdictional authorities to ensure the provided plan will reduce traffic during ingress and egress. The Lantern Fest will ensure that proper law enforcement officials are at the sole freeway exit to manage traffic on to I-80.

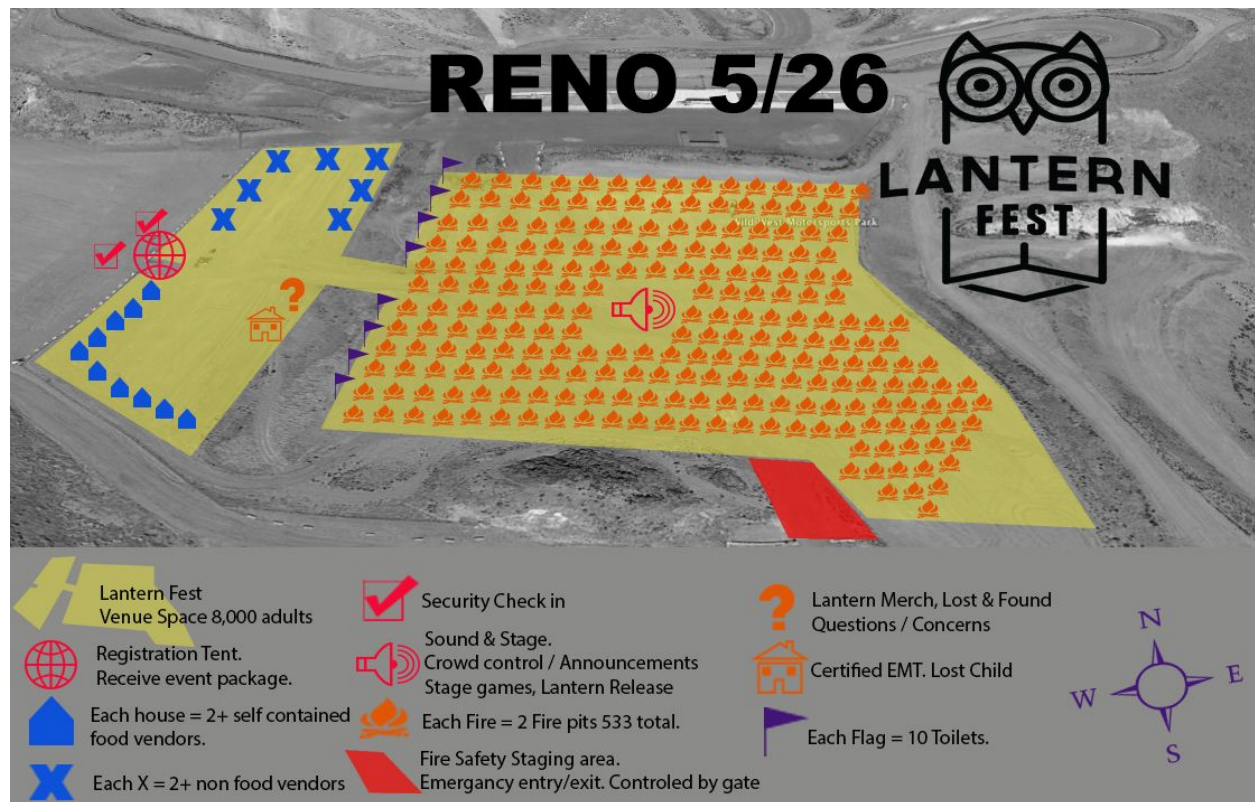
Appendix G

Vehicle Access and on-site traffic control



Please see Appendix G. The Lantern Fest is obligated to follow the Vehicle Access and on-site traffic control plan previously approved by the county for racing events that take place at The WildWest Motorsports Park. The Lantern Fest promises to follow such plan and work with jurisdictional authorities to ensure the plan appropriately addresses the needs of this specific event.

Communication System



The Lantern Fest provides a circular stage hosted by an MC at every event. The stage allows The Lantern Fest to communicate with every participant in a timely and effective manner. Local law enforcement and fire officials are provided with dedicated radios that allow them to communicate directly with both the MC and the event director. Every employee of The Lantern Fest is provided with a radio and able to communicate directly with each other as well as fire and law enforcement officials.

Appendix I

Illuminating the premises

The Lantern Fest will provide, at a minimum, 6 portable light stands that provide reasonable and appropriate lighting for the entire venue, parking areas, and exits. The Lantern Fest will ensure that all exits are appropriately lit during the duration of the event.

Appendix J

Clean-up

The Lantern Fest begins cleaning the venue shortly after participants begin to leave. The entire area is returned to its original form by noon the day after the event. The Lantern Fest leases all appropriate waste disposal facilities needed to do this.

Appendix K



CERTIFICATE OF LIABILITY INSURANCE

DATE (MM/DD/YYYY)

02/27/2018

THIS CERTIFICATE IS ISSUED AS A MATTER OF INFORMATION ONLY AND CONFERS NO RIGHTS UPON THE CERTIFICATE HOLDER. THIS CERTIFICATE DOES NOT AFFIRMATIVELY OR NEGATIVELY AMEND, EXTEND OR ALTER THE COVERAGE AFFORDED BY THE POLICIES BELOW. THIS CERTIFICATE OF INSURANCE DOES NOT CONSTITUTE A CONTRACT BETWEEN THE ISSUING INSURER(S), AUTHORIZED REPRESENTATIVE OR PRODUCER, AND THE CERTIFICATE HOLDER.

IMPORTANT: If the certificate holder is an ADDITIONAL INSURED, the policy(ies) must be endorsed. If SUBROGATION IS WAIVED, subject to the terms and conditions of the policy, certain policies may require an endorsement. A statement on this certificate does not confer rights to the certificate holder in lieu of such endorsement(s).

PRODUCER Western States Insurance Agency Inc 87 East Center Spanish Fork, UT, 84660 License #: 92455		CONTACT NAME: Shantelle Martinez PHONE: (801)798-7461 FAX: (801)798-7462 E-MAIL: shantelle@westernstatesinsurance.net ADDRESS: shantelle@westernstatesinsurance.net	
INSURED Lantern Fest Productions; Happy Run Events LLC; & Sack Lunch Eric Brooks 59 W 100 S Salt Lake City UT 84101		INSURER(S) AFFORDING COVERAGE INSURER A: Underwriters at Lloyds INSURER B: INSURER C: INSURER D: INSURER E: INSURER F:	

COVERAGES

CERTIFICATE NUMBER:

REVISION NUMBER:

THIS IS TO CERTIFY THAT THE POLICIES OF INSURANCE LISTED BELOW HAVE BEEN ISSUED TO THE INSURED NAMED ABOVE FOR THE POLICY PERIOD INDICATED. NOTWITHSTANDING ANY REQUIREMENT, TERM OR CONDITION OF ANY CONTRACT OR OTHER DOCUMENT WITH RESPECT TO WHICH THIS CERTIFICATE MAY BE ISSUED OR MAY PERTAIN, THE INSURANCE AFFORDED BY THE POLICIES DESCRIBED HEREIN IS SUBJECT TO ALL THE TERMS, EXCLUSIONS AND CONDITIONS OF SUCH POLICIES. LIMITS SHOWN MAY HAVE BEEN REDUCED BY PAID CLAIMS.

INSR LTR	TYPE OF INSURANCE	ADDL SUBR INSD: WVD	POLICY NUMBER	POLICY EFF (MM/DD/YYYY)	POLICY EXP (MM/DD/YYYY)	LIMITS
A	<input checked="" type="checkbox"/> COMMERCIAL GENERAL LIABILITY		LF000-1000081	03/17/2018	03/18/2018	EACH OCCURRENCE \$ \$6,000,000
	<input checked="" type="checkbox"/> CLAIMS-MADE <input type="checkbox"/> OCCUR					DAMAGE TO RENTED PREMISES (Ea occurrence) \$ \$100,000
						MED EXP (Any one person) \$ \$25,000
						PERSONAL & ADV INJURY \$ \$6,000,000
	GEN'L AGGREGATE LIMIT APPLIES PER: <input checked="" type="checkbox"/> POLICY <input type="checkbox"/> PROJECT <input type="checkbox"/> LOC OTHER:					GENERAL AGGREGATE \$ \$6,000,000
						PRODUCTS - COMP/OP AGG \$ \$6,000,000
	AUTOMOBILE LIABILITY					
	<input type="checkbox"/> ANY AUTO					COMBINED SINGLE LIMIT (Ea accident) \$
	<input type="checkbox"/> ALL OWNED AUTOS					BODILY INJURY (Per person) \$
	<input type="checkbox"/> HIRED AUTOS					BODILY INJURY (Per accident) \$
	<input type="checkbox"/> SCHEDULED AUTOS					PROPERTY DAMAGE (Per accident) \$
	<input type="checkbox"/> NON-OWNED AUTOS					
	UMBRELLA LIAB					
	<input type="checkbox"/> EXCESS LIAB					EACH OCCURRENCE \$
	<input type="checkbox"/> RETENTION \$					AGGREGATE \$
	<input type="checkbox"/> WORKERS COMPENSATION AND EMPLOYERS' LIABILITY					
	<input type="checkbox"/> ANY PROPRIETARY PARTNER/EXECUTIVE OFFICER/MEMBER EXCLUDED? (Mandatory in NH)					PER STATUTE \$
	<input type="checkbox"/> If yes, describe under DESCRIPTION OF OPERATIONS below					OTH-ER \$
						E.L. EACH ACCIDENT \$
						E.L. DISEASE - EA EMPLOYEE \$
						E.L. DISEASE - POLICY LIMIT \$

DESCRIPTION OF OPERATIONS / LOCATIONS / VEHICLES (ACORD 101, Additional Remarks Schedule, may be attached if more space is required)

The certificate holder is listed as an additional insured for this event.
Retro Date Reporting Period: 36 Months
Waiver of Subrogation applies, blanket additional insured endorsement is attached.

CERTIFICATE HOLDER**CANCELLATION**

SHOULD ANY OF THE ABOVE DESCRIBED POLICIES BE CANCELLED BEFORE THE EXPIRATION DATE THEREOF, NOTICE WILL BE DELIVERED IN ACCORDANCE WITH THE POLICY PROVISIONS.

AUTHORIZED REPRESENTATIVE

NM 87171

ACORD 25 (2014/01)

© 1988-2014 ACORD CORPORATION. All rights reserved.
The ACORD name and logo are registered marks of ACORD

To whom it may concern the attached report is pertaining to the flight characteristics of the Lantern used in the LANTERN FEST. Testing of lantern were conducted to obtain the following data:

- How long does the lantern burn
- What is the max temperature of the fuel cell as it burns
- How far the lantern travel at different air speeds
- How high does the lantern go

The report address the obtained data. Mathematical equations were developed to predict the ascend rate and the descend rate of the lantern at different locations.

The testing, data analysis, and mathematic equations were done by Kerm Jackson. Kerm is a Professional Engineer in the State of Utah. He has worked as a mechanical engineer for over 30 years. He has designed many furnace exhaust system and building ventilation systems. This work used air density and air flow rates to design the exhaust fans and ventilation blowers. Research on the flight of hot air balloons and weather balloons was conducted. This research lead to the mathematic equations.

Thanks,

Kerm Jackson

634 East 920 North,

Orem, Utah 84097

801-592-4941



Flight Characteristics of the Lantern of LANTERN FEST

Testing of lantern was conducted to obtain the following data:

- How long does the lantern burn
- What is the max temperature of the fuel cell as it burns
- How high does the lantern go
- How far the lantern travel at different air speeds

Testing was done in Orem, Utah November 22, 2016. The temperature was cool and no detectable wind. The maximum temperature testing was conducted in two-car garage. The flight testing was conducted in a large open playing field.

The Lanterns were tested to determine the time the fuel cell burns. The burn time was about 3 minutes. It takes the first minute to inflate the canopy sufficient to lift the lantern to flight status. The next two minutes while the fuel cell burned the lantern ascended. The maximum temperature inside the canopy was about 300° F. This temperature was used as the hot air temperature inside the lantern canopy. In the two minutes the lantern reached an altitude of about 600 feet.

The lantern descends for about three minutes. The flights of the lanterns varied from four minutes to six minutes. One lantern ascended for two minutes and then continued ascend and to be carried by the wind until the lantern was out of sight.

A paper named “Modeling the ascent of sounding balloons: derivation of the vertical air motion” developed equations for a helium weather balloon. This paper was placed in Appendix 4. The ascent equation was starting point for the mathematical equation for the ascent of the lantern. The equation was modified to match the data for the lantern. The drag force equation was modified to predict the descend rate of the lantern. The equations used the density of the air to predict the rate of rise and the rate of falling at different locations.

Devices similar to the lanterns are used to measure the wind speed. The Lanterns travel at the wind speed. Wind at one mile per hour calculates to 1.46 feet per second. The Lantern ascends for about two minutes and descends for about three minutes. In five minutes at 1.46 ft/sec the lantern travels 440 feet. The following table lists the wind speed and the horizontal distance the lantern travels in five minutes

1 MPH	440 FT
2 MPH	880 FT
3 MPH	1320 FT
4 MPH	1760 FT

5 MPH 2200 FT

6 MPH 2460 FT

An Excel spread sheet was developed to calculate the ascend and descend rates of the lantern at different elevations, air temperatures, and relative humidity. This Excel spread sheet is printed and attached as Appendix 1. The EXCEL spread sheet is provided as an attachment. The air density is calculated by the Air Density Calculator. A printed version of this calculator is in Appendix 2. The Air Density Calculator is provided as an attachment. The air density is transferred to the Excel spread sheet. Embedded calculations predict the ascend and descend rates. The embedded equations are shown on the spread sheet.

Hand written data sheets and sample calculations are attached as Appendix 3. The handwritten calculations define the elements of the equations. A copy of the embedded calculation is presented.

Appendix 1

LANTERN FEST

The Lanterns burn for about 3 minutes.

It takes the first minute to inflate the canopy sufficient to lift the lantern to flight status

The maximum temperature inside the canopy is 300° F

The lantern ascends for about two minutes to an altitude of about 600 feet

The lantern descends for about three minutes.

Lantern Ascent rate and Descend rate

Testing was done in Oerm, Utah November 22, 2016

Air Temperature :	53 ° F	11.7 ° C
Humidity	43 %	
Elevation	4774 FT	1455 M
Ambient air density		from the Air Density Program using
	0.0671 LB/FT ³	conditions at the launch site
Hot Air Temperature	300 ° F	148.9 ° C
Humidity	0 %	Air above 212° F contains no humidity
Elevation	4774 FT	1455 M
Hot air density		from the Air Density Program using
	0.0437 LB/FT ³	conditions at the launch site with air
		temperature 300° F and no humidity
Ascent Rate Formula:	$v = ((76.4/4.3) * (3 * (((C16 - C20) * 6.06) + 0.118))) / (8.85 / C16)^{0.5}$	
Ascent rate	4.83 ft/sec	
Descend Rate Formula:	$v = (((((C16 - C20) * 6.06) + 0.118) * 2 / 0.3 / C16 / 2.49)^{0.5})$	
Decent rate	3.22 ft/sec	

Wind Speed

Devices similar to the Lanterns are used to measure the wind speed.

The Lanterns travel at the wind speed.

Wind at one mile per hour calculates to 1.46 feet per second.

The Lantern ascends for about two minutes and descends for about three minutes.

In five minutes at 1.46 ft/sec the lantern travels 440 feet

The following table lists the wind speed and the horizontal distance the lantern travels in five minutes

1 MPH	440 FT
2 MPH	880 FT
3 MPH	1320 FT
4 MPH	1760 FT
5 MPH	2200 FT
6 MPH	2640 FT

Example Conditions

Lantern Ascent rate and Descend rate

Chicago, IL

Air Temperature :	95 ° F	35.0 ° C
Humidity	90 %	
Elevation	600 FT	183 M
Ambient air density		from the Air Density Program using conditions at the launch site
	0.0686 LB/FT ³	
Hot Air Temperature	300 ° F	148.9 ° C
Humidity	0 %	Air above 212° F contains no humidity
Elevation	600 FT	183 M
Hot air density		from the Air Density Program using conditions at the launch site with air temperature 300° F and no humidity
	0.05109 LB/FT ³	
Ascent Rate Formula:	$v = ((76.4/4.4) * (3 * (((C16 - C20) * 6.06) + 0.118)) / 8.85 / C16)^{0.5}$	
Ascent rate	4.43 ft/sec	
Descend Rate Formula:	$v = (((((C16 - C20) * 6.06) + 0.118) * 2) / 0.03 / 2.49 / 0.671)^{0.5}$	
Decent rate	2.96 ft/sec	

Los Angeles, CA

Air Temperature :	70 ° F	21.1 ° C
Humidity	15 %	
Elevation	600 FT	183 M
Ambient air density		from the Air Density Program using conditions at the launch site
	0.07223 LB/FT ³	
Hot Air Temperature	300 ° F	148.9 ° C
Humidity	0 %	Air above 212° F contains no humidity
Elevation	600 FT	183 M
Hot air density		from the Air Density Program using conditions at the launch site with air temperature 300° F and no humidity
	0.05109 LB/FT ³	
Ascent Rate Formula:	$v = ((76.4/4.4) * (3 * (((C16 - C20) * 6.06) + 0.118)) / 8.85 / C16)^{0.5}$	
Ascent rate	4.53 ft/sec	
Descend Rate Formula:	$v = (((((C16 - C20) * 6.06) + 0.118) * 2) / 0.03 / 2.49 / 0.671)^{0.5}$	
Decent rate	3.02 ft/sec	

Appendix 2

Please fill all required fields

OK

Air Density Calculator

Altitude, Temperature, Humidity and Barometric Pressure of Weather Systems and their impact on local atmospheric air density.

For accurate measurement of local air conditions we recommend a high accuracy & robust [logging weather station](#) such as the ones sold on [Wind101.Com](#) and [Wind101.Net](#) live streaming weather portal.

AIR DENSITY CALCULATION INPUTS
(local atmospheric conditions)

Property	Value	Unit of Measure	Alternate Units	Description / Note
Air Temperature =	33.0	C (degrees)	0 F (degrees)	Local air temperature
Air Humidity =	90	% (Rel. Humidity)	0 g/m3 (ABS Humidity)	Relative and corresponding Absolute Humidity value.
*Barometric Pressure =	1013.25	hPa (hecto-Pascals)	0 mmHg (mm of Mercury)	*If pressure value is set to "0", Altitude value is used to calculate local barometric pressure based on the 1976 Standard Atmosphere Model .
Altitude / Elevation =	500	meters	0 ft	Altitude above Sea Level /elevation
AIR DENSITY CALCULATOR OUTPUT				
**Air Density =	0	kg/m3	0 lb/ft3	Local air density corrected for local altitude, temperature, humidity and barometric pressure.
**Local air density is a very important factor in determining wind turbine performance and engine horse power output. Each factor like altitude above sea level, air temperature, humidity, and even barometric pressure due to local weather systems can have significant effect on local air density.				
**Thus, if one wants to accurately predict wind turbine performance, it is not only important to use an accurate anemometer to measure wind speed, but to also measure all the other atmospheric factors which can have up to 10% influence on wind energy calculations.				
***Dew Point Air Temperature =	0	C (degrees)	0 F (degrees)	Air temperature at which air humidity starts to condense into water droplets.
***If an object at this temperature is located in the air environment of the above given conditions, the object, like a car window, will fog up due to air humidity condensing on its surface.				



equation 4b

$\rho = 0$ kg/m3 air density corrected for altitude, temperature and pressure
 $\rho_{corrected} = 0$ kg/m3 air density corrected for altitude, temperature, pressure and humidity.
D = density, kg/m3
 P_d = pressure of dry air (partial pressure), Pascals
 P_v = pressure of water vapor (partial pressure), Pascals
 $P = P_d + P_v$ = total air pressure, Pascals (multiply mb by 100 to get Pascals)
 $R_d = 287.05$ gas constant for dry air, J/(kg*degK) = 287.05 = R/Md
 $R_v = 461.495$ gas constant for water vapor, J/(kg*degK) = 461.495 = R/Mv
 $R = 814.37$ universal gas constant = 814.37 (in 1976 Standard Atmosphere)
 $M_d = 28.964$ molecular weight of dry air = 28.964 gm/mol
 $M_v = 18.016$ molecular weight of water vapor = 18.016 gm/mol
 T = temperature, deg K = deg C + 273.15

Standard Atmosphere

p0= 101325 Pa
T0= 288.15 K
rho0= 1.225 kg/m3

To calculate the density of air as a function of altitude, one requires additional parameters. They are listed below, along with their values according to the [International Standard Atmosphere](#), using the [universal gas constant](#) instead of the specific one:

Temperature at altitude h meters above sea level is given by the following formula (only valid inside the troposphere):

T standard = 0	K
T Non-standard = 0	K

$$p = p_0 \cdot \left(1 - \frac{g_0}{R \cdot T_0} h\right)^{\frac{R \cdot T_0}{g_0}}$$

pressure at altitude

$\frac{g_0 \cdot M}{R \cdot T_0} = 0$
p = 0 Pa

rho =

density can then be calculated according to this molar form formula

PENFED CREDIT UNION

HARVEST A GREAT LOW MORTGAGE RATE

Our 30-year fixed mortgage is available with a 60-day rate lock

3.875% RATE
3.999% APR

LEARN MORE

$\rho = 0$	kg/m3	
$\rho_{non_std_temp} = 0$	kg/m3	

Temp = 0	C	ambient temperature
h = 0	meters	Altitude above sea level
p0 = 101325	Pa	sea level standard atmospheric pressure
T0 = 288.15	K	sea level standard temperature
g = 9.80665	m/s2	Earth-surface gravitational acceleration
L = 0.0065	K/m	temperature lapse rate
R = 8.31447	J/(mol·K)	universal gas constant
M = 0.0289644	kg/mol	molar mass of dry air

Es = 0	Pascals (Pa)	equation 6	saturation
Tc = 0	temperature, deg C	pressure of water vapor	
c0 = 6.1078			
c1 = 7.5			
c2 = 237.3			

Pv = Rh*Es		actual water vapor pressure	
Pv = 0			
Es = 0			
RH % = 0			

P @ Alt & Temp = 0	Pascals (Pa)	actual water vapor pressure	
P = 0	Pascals (Pa)	absolute atmospheric pressure	
h = 0	meters	altitude above Sea Level	

Density correction for humidity multiplier = 0	ratio		
--	-------	--	--

td = 243.12*(H/(17.62-H))	°C		
H = ((log10(RH)-2.0)/0.4343+(17.62*T))/(243.12+T)			
td = 0	°C	dew Point Temperature	
H = 0			
RH % = 0			
Temp = 0			
m = 17.62			
Tn = 243.12	°C		
A = 6.112	hPa		

dv = 0	g/m3		absolute
--------	------	--	----------

Humidity



[Click for Professional accuracy anemometer and weather station sales](#)
Copyright Barani Design and Barani Design sro © 2012

Appendix 3

Project No. LANTERN FEST Date: 11-17-16 Calc No.: _____

Author: KJACKSON Check: _____ Sheet 1 of 5

Title: _____

RING $14\frac{1}{2}" \times 13\frac{3}{4}"$
HEIGHT $29\frac{1}{2}"$
CANOPY SQUARE $19" \times 19"$

VOLUME OF CANOPY

$$\text{RECTANGLE } 19 \times 19 \times 29\frac{1}{2} = 10649.5 \text{ IN}^3 \\ = 6.16 \text{ FT}^3$$

$$\text{CANOPY VOLUME} = 6.06 \text{ FT}^3$$

$$\text{CANOPY AREA} = 19" \times 19" = 361 \text{ IN}^2$$

SPHERE RADIUS:

$$A = \frac{\pi D^2}{4} = 361 \text{ IN}^2$$

$$D^2 = 460 \text{ IN}^2$$

$$D = 21.4 \text{ IN}$$

$$D = 1.79 \text{ FT}$$

$$R = 0.89 \text{ FT}$$

Project No. LANTER FEST Date: 11-17-16 Calc No.: _____

Author: K JACKSON Check: _____ Sheet 2 of 5

Title: _____

SCALE ± 0.1 GRAM

CUP 142.8 142.9 142.9 142.9 142.8

LANTERNS 1 408.0 407.9 408.2 408.4

LANTERNS & BAG 1 143.0 143.0 143 143.1
416.1 416.1 416.2 416.0

LANTERNS & BAG 2 142.7 142.5 142.6 142.6
420.6 420.6 420.5 420.5

LANTERNS 1 $408.1 - 142.9 = 265.2$

BAG 1 $416.1 - 408.1 = 8$

LANTERNS 2 $420.6 - 8 = 412.6 - 142.6 = 270$

10 LANTERNS = $265.2 + 270 = 535.2$

1 LANTERN = $535.2 \div 10 = 53.5$ GRAMS

53.5 GRAMS $\frac{2.2 \text{ LBS}}{1000 \text{ GRAMS}} = 0.118 \text{ LBS}$

ONE LANTERN = 0.118 LBS

Project No. LANTERN FEST Date: 11-25-16 Calc No.: _____

Author: K JACKSON Check: _____ Sheet 3 of 5

Title: _____

ASCENT RATE EQUATION WAS MODIFIED AS FOLLOWS

$$V_2 = \sqrt{\frac{8Rg}{3C_D} \left(\frac{3m_{TOT}}{4\pi\rho_a R^3} \right)}$$

R = RADIUS OF THE SPHERE

R = 0.89 FT (SHEET 1)

g = ACCELERATION DUE TO GRAVITY

g = 32.2 FT/SEC²

C_D CALCULATED FROM EXPERIMENTAL DATA

$$m_{TOT} = m_{LIFTAIR} + m_{LANTERN}$$

CANOPY VOLUME = 6.06 FT³ (SHEET 1) C_D = DRAG FORCE

AMBIENT AIR DENSITY 0.0671 LBS/FT³ C_D = 4.3 (NO UNITS)

AIR DENSITY CALCULATOR
TEMP 53°F = 11.7°C
HUMIDITY 43%
ELEVATION 4,774 FT = 1455 M

m_{TOT} = BALLOON TOTAL MASS

HOT AIR DENSITY 0.00395 LBS/FT³

m_{LANTERN} = 0.118 LBS (SHEET 2)

AIR DENSITY CALCULATOR
TEMP 300°F = 150°C
HUMIDITY 43%
ELEVATION 4,774 FT = 1455 M

ρ_a = AMBIENT AIR DENSITY

ρ_a = 0.0671 LBS/FT³

ρ_H = HOT AIR DENSITY

ρ_H = 0.0437 LBS/FT³

$$m_{LIFT} = (\rho_a - \rho_H) 6.06 \text{ FT}^3$$

$$m_{LIFT} = (0.0671 - 0.0437) \frac{\text{LBS}}{\text{FT}^3} (6.06 \text{ FT}^3)$$

$$m_{LIFT} = 0.142 \text{ LBS}$$

V₂ = BALLOON ASCENT RATE

$$V_2 = \frac{\text{FT}}{\text{SEC}}$$

$$m_{TOT} = m_{LANTERN} + m_{LIFT}$$

$$m_{TOT} = 0.142 \text{ LBS} + 0.118 \text{ LBS}$$

Project No. LANTERN FEST Date: 11-25-16 Calc No.: _____

Author: K JACKSON Check: _____ Sheet 4 of 5

Title: _____

$$M_{TOT} = 0.260 \text{ LBS}$$

$$N_2 = \sqrt{\frac{8(0.89)(32.2)}{3(4.3)} \left(\frac{3(0.260)}{4\pi(0.0671)(0.89)^3} \right)}$$

$$N_2 = \sqrt{17.4 \left(\frac{0.78}{0.594} \right)}$$

$$\sqrt{17.4 (1.31)}$$

$$N_2 = 4.8$$

Project No. LANTERN FEST Date: 11-25-16 Calc No.: _____

Author: K JACKSON Check: _____ Sheet 5 of 5

Title: _____

DESCENT FORMULA WAS MODIFIED

$$F_D = \frac{1}{2} C_D \rho_a S v_z^2$$

$$v_z^2 = \frac{F_D}{C_D \rho_a S}$$

F_D WAS SUBSTITUTED FOR
 M_{TOT}
 $S = (\pi R^2)$

$$M_{TOT} = 0.260 \text{ LBS (SHAFT 4)}$$

C_D = CALCULATED FROM
EXPERIMENTAL DATA

$$C_D = 0.3$$

$$v_z^2 = \frac{(0.260 \text{ LBS})^2}{(0.3 \text{ SEC}) \left(\frac{0.671 \text{ LBS}}{\text{FT}^3} \right) \pi (0.89)^2 \text{ FT}^2}$$

$$v_z^2 = \frac{0.52}{(0.3) (2.49) (0.0671)}$$

$$v_z = 3.22 \text{ FT/SEC}$$

F_D = DRAG FORCE

= LBSF

C_D = DRAG COEFFICIENT

= 0.3 SEC

ρ_a = AMBIENT AIR
MASS DENSITY

$$\rho_a = 0.0671 \frac{\text{LBS}}{\text{FT}^3}$$

S = CROSS-SECTIONAL
AREA OF THE SPHERE

$$S = \pi R^2$$

$$R = 0.89 \text{ FT}$$

v_z = DESCENT RATE

$$v_z = \text{FT/SEC}$$

Appendix 4

Modeling the ascent of sounding balloons: derivation of the vertical air motion

A. Gallice¹, F. G. Wienhold¹, C. R. Hoyle^{1,*}, F. Immler², and T. Peter¹

¹Institute for Atmospheric and Climate Science, Swiss Federal Institute of Technology, Zurich, Switzerland

²Richard Assmann Observatory, German Meteorological Service (DWD), Lindenberg, Germany

*now at: Laboratory of Atmospheric Chemistry, Paul Scherrer Institut, Villigen, Switzerland

Received: 3 June 2011 – Published in Atmos. Meas. Tech. Discuss.: 23 June 2011

Revised: 21 September 2011 – Accepted: 6 October 2011 – Published: 20 October 2011

Abstract. A new model to describe the ascent of sounding balloons in the troposphere and lower stratosphere (up to ~30–35 km altitude) is presented. Contrary to previous models, detailed account is taken of both the variation of the drag coefficient with altitude and the heat imbalance between the balloon and the atmosphere. To compensate for the lack of data on the drag coefficient of sounding balloons, a reference curve for the relationship between drag coefficient and Reynolds number is derived from a dataset of flights launched during the Lindenberg Upper Air Methods Inter-comparisons (LUAMI) campaign. The transfer of heat from the surrounding air into the balloon is accounted for by solving the radial heat diffusion equation inside the balloon. In its present state, the model does not account for solar radiation, i.e. it is only able to describe the ascent of balloons during the night. It could however be adapted to also represent daytime soundings, with solar radiation modeled as a diffusive process. The potential applications of the model include the forecast of the trajectory of sounding balloons, which can be used to increase the accuracy of the match technique, and the derivation of the air vertical velocity. The latter is obtained by subtracting the ascent rate of the balloon in still air calculated by the model from the actual ascent rate. This technique is shown to provide an approximation for the vertical air motion with an uncertainty error of 0.5 m s^{-1} in the troposphere and 0.2 m s^{-1} in the stratosphere. An example of extraction of the air vertical velocity is provided

in this paper. We show that the air vertical velocities derived from the balloon soundings in this paper are in general agreement with small-scale atmospheric velocity fluctuations related to gravity waves, mechanical turbulence, or other small-scale air motions measured during the SUCCESS campaign (Subsonic Aircraft: Contrail and Cloud Effects Special Study) in the orographically unperturbed mid-latitude middle troposphere.

1 Introduction

Sounding balloons are extensively used in meteorological forecasting and research, to the extent that several hundreds of them are sent daily into the atmosphere worldwide. They are mostly used to carry radiosondes aloft, enabling for the in situ recording of atmospheric variables with high temporal frequency and precision. This measurement technique stands among the most popular, for it is not subject to the same limitations as the majority of remote sensing instruments, such as decreasing accuracy with altitude or susceptibility to cloud cover.

Despite the wide usage of sounding balloons, rather limited effort has been put into the detailed modeling of their ascent. This results originally from the practice of storing radiosonde temperature, wind and humidity data only on a small number of so-called mandatory and significant levels (Alexander et al., 2010) with very coarse vertical resolution. Yet, for special cases radiosonde vertical ascent velocities have been analyzed in detail; e.g. Shutts et al. (1988) calculated the momentum flux of a single strong gravity wave



Correspondence to: A. Gallice
(aurelien.gallice@gmail.com)

from fluctuations in balloon ascent velocities. However, Zink and Vincent (2001) state that smaller fluctuations can be due to measurement errors of radiosonde altitude or changing drag coefficient of the balloon, and recommend to calculate the vertical perturbation velocity from observed temperature fluctuations, assuming the intrinsic frequency of the contributing waves to derive the vertical momentum flux. Their statement nevertheless lacks support by evidences, and we expect their method to provide a low-accuracy estimation of the vertical air motion.

In an effort to obtain information also about atmospheric smaller scale wave activity the World Climate Research Program's (WCRP's) Stratospheric Processes and their Role in Climate (SPARC) project started to save the high-resolution radiosonde data (Hamilton and Vincent, 1995), archiving them at the SPARC Data Center.¹ Still, a general modeling approach for radiosonde ascents in dependence on the state of the atmosphere is lacking.

A coarse modeling approach for sounding balloon ascents assuming constant ascent velocities has been used recently to improve the precision of the "match" technique (Engel, 2009). The latter consists in probing the same air parcel twice using two sounding balloons launched at different times (typically a few hours apart) and locations (typically tens to hundreds of kilometers apart) in order to obtain information on the time evolution of the air parcel's properties, e.g. with respect to gases, aerosols or cloud particles. The match technique has been used in the past to compute ozone loss rate in the lower stratosphere at the poles (Rex et al., 1999), but the ozone match flights did not rely on the use of a balloon ascent model; the procedure consisted in launching the first balloon, then precisely forecasting the trajectories of the air parcels measured by the ozone sonde, and finally launching a second balloon from a location downstream in order to measure the air parcel a second time. In order to improve the quality for the match by the second sounding, a new procedure involving balloon ascent modeling has been proposed recently (Engel, 2009). Assuming a constant ascent rate of 5 m s^{-1} for the balloon superimposed on weather forecast or analysis data, this technique is currently used to study the evolution of supersaturations of water vapor with respect to ice in cirrus clouds, which should eventually lead to a better understanding of the role of cirrus clouds in climate change.

As the interest in sounding balloon modeling has rejuvenated only recently, there are surprisingly few more precise model attempts. One is the model recently proposed by Wang et al. (2009) enabling the extraction of the air vertical velocity from radiosonde data. Their method is based on a decomposition of the balloon ascent rate into a contribution representing the balloon ascent in still air and a contribution representing vertical air motion. The balloon ascent rate in the absence of vertical winds is computed using a model and

the radiosonde data. Air vertical velocity is then obtained by subtracting the ascent rate in still air from the actual ascent rate. Wang et al. discuss the advantages of this method over other techniques aimed at deriving the air vertical velocity. Their model for the ascent of a sounding balloon in still air is based on the balloon's momentum conservation equation. From this equation, they obtain an expression of the balloon ascent rate in still air as a function of the balloon volume and of the drag coefficient. The balloon volume change with altitude is computed from the balloon volume at ground by assuming thermal equilibrium with ambient air at all times during the ascent. The values of the drag coefficient – taken as constant above 5 km altitude – and of the balloon volume at ground are optimized for each flight so as to minimize the median departure of the modeled ascent rate in still air from the actual ascent rate.

Other ascent models have been developed for different types of balloons, especially zero-pressure balloons (Musso et al., 2004; Palumbo, 2007). These models often involve a thorough treatment of the radiative and convective transport of heat inside the balloon. The most advanced ones take geometric factors and the variation of the balloon drag coefficient with altitude into account (Palumbo, 2007). These models can, however, not be applied to the case of sounding balloons, since they rely on empirical relations – relating for example the drag coefficient to the Reynolds and Froude numbers – which are valid for zero-pressure balloons only. As a matter of fact, the latter differ from the sounding balloons with respect to at least two important points: (a) their size and their payload weight are of the order of 30 to 70 times higher, hereby providing them a much stronger inertia and diminishing consequently their sensibility to atmospheric disturbances; and (b) their envelope is not close to spherical but rather of a much more complex shape, thereby significantly influencing the dynamics of their drag coefficient.

In the present work, a model for the ascent of a sounding balloon in still air is developed, going beyond the work by Wang et al. (2009) by taking into account both the variation of the balloon drag coefficient with altitude and the heat imbalance between the balloon and the ambient air. In order to keep the model manageable, three major assumptions are made. Firstly, the balloon is approximated by an almost spherical bubble of gas, the latter being assumed to follow the ideal gas law. This approximation subtends that the balloon envelope is not resolved in the model, which implies that the pressure inside and outside of the balloon are considered to be equal. It should be noted that the balloon shape is not restricted to a perfect sphere so as to account for the effect of the air flow around the balloon and the presence of the payload. Secondly, it is assumed that the process responsible for the propagation of heat inside the balloon can be described as diffusion. This comprises not only molecular diffusion, but also convection and radiative heat transfer, which are both assumed to be representable by diffusive

¹<http://www.sparc.sunysb.edu/html/hres.html>

laws. One consequence of this approximation is that only night flights can be modeled accurately. Thirdly, the temperature distribution inside the balloon is assumed to be spherically symmetric. The permissibility of this approximation is granted by the fact that deviations of the balloon shape from spherical remain limited. Despite these assumptions, the present model is expected to enable more precise balloon trajectory forecasts and characterizations of the air vertical velocity than other currently available models.

The theoretical background underpinning the balloon ascent model is developed in Sect. 2. In Sect. 3, the ascent model is described in detail. Its evaluation and a discussion of its application to the derivation of the air vertical velocity are presented in Sect. 4. Section 5 provides a conclusion and a discussion of potential improvements to the present model.

2 Theoretical background

2.1 Balloon ascent rate

The expression of the ascent rate of the balloon in still air is derived from the balance between the “free lift”, F_{FL} , and the drag force, F_D (Wang et al., 2009). The free lift corresponds to the net upward force acting on the balloon and is expressed as the difference between the buoyancy force and the total weight of the balloon (Yajima et al., 2009),

$$F_{FL} = (\rho_a V - m_{tot})g, \quad (1)$$

where ρ_a denotes the ambient air mass density, V the balloon volume, m_{tot} the balloon total mass – namely the sum of the respective masses of the balloon envelope, of the lifting gas and of the payload – and g the acceleration due to gravity at the surface of the Earth. The expression for the drag force in still air reads

$$F_D = \frac{1}{2} c_D \rho_a S v_z^2, \quad (2)$$

where c_D refers to the drag coefficient, S to the reference area and v_z to the balloon ascent rate in still air. The reference area can be chosen arbitrarily, so that c_D is a priori not uniquely defined for a given drag force. In this study, S is chosen as the cross-sectional area of the sphere with same volume as the balloon. This choice follows the standard definition of the reference area for non-spherical objects (Loth, 2008). The advantage of this choice is that the departure of the balloon shape from spherical is entirely captured and described by the drag coefficient only. Denoting by R the radius of the volume-equivalent sphere, S and V can be written as: πR^2 and $(4/3)\pi R^3$, respectively.

The expression of v_z is obtained by equating Eqs. (1) and (2),

$$v_z = \sqrt{\frac{8Rg}{3c_D} \left(1 - \frac{3m_{tot}}{4\rho_a R^3} \right)}, \quad (3)$$

where V and S have been replaced by their respective expressions as a function of the volume-equivalent sphere radius, R , hereafter called “balloon effective radius.” Provided that m_{tot} is known and that ρ_a can be determined using either a numerical weather forecast (in the case of Eq. (3) being used to forecast the balloon trajectory) or using the radiosonde data recorded during the balloon ascent (in the case of Eq. (3) being used a posteriori for the derivation of the vertical air motion), the computation of v_z from Eq. (3) still requires the knowledge of R and c_D . The balloon effective radius, as a result of the decreasing ambient air pressure, increases during the balloon ascent. If the expansion of the balloon volume was treated as a purely adiabatic process, the temperature difference between the ambient air and the balloon would continue to increase with altitude, for the environmental lapse rate is smaller than the adiabatic lapse rate. As a consequence, heat transfer from the ambient air into the balloon must also be taken into account if the variation of the balloon volume with altitude is to be determined physically. Heat transfer is resolved in the present case by solving the radial heat diffusion equation inside the balloon with a prescribed Dirichlet boundary condition at the balloon surface, as discussed in more detail in Sect. 2.2. The dynamics of the drag coefficient are discussed in Sect. 2.3.

2.2 Heat diffusion inside the balloon

The variation of the balloon effective radius (R) with altitude results from both adiabatic expansion and heat transfer from the surrounding air into the balloon. The heat flux at the balloon surface is assumed to propagate inside the balloon volume by means of diffusion (see Sect. 1). In our model applications we restrict heat diffusion to be only molecular; the case where also eddy diffusion or convection are assumed to take place is discussed in Sect. 5. The temperature distribution inside the balloon, $T_b(r, t)$, is assumed to be spherically symmetric and therefore to obey the radial heat diffusion equation (Carslaw and Jaeger, 1959),

$$\frac{\partial T_b}{\partial t} = \frac{\langle D \rangle}{R^2} \frac{1}{r^2} \frac{\partial}{\partial r} \left(r^2 \frac{\partial T_b}{\partial r} \right), \quad (4)$$

where $\langle D \rangle = \langle \kappa / (\rho_b c_p) \rangle$ is the mean molecular heat diffusion coefficient averaged over the balloon volume, $r \in [0, 1]$ denotes the radial coordinate non-dimensionalized by the balloon effective radius (R) and t refers to time. The normalization of the radial coordinate by R simplifies the discussion of the model in Sect. 3. In the expression for the mean molecular heat diffusion coefficient, κ refers to the lifting gas thermal conductivity, which is a known function of T_b (see e.g. Vargaftik et al., 1994, for the thermal conductivity of hydrogen and helium), ρ_b denotes the lifting gas mass density, deduced from T_b and the pressure using the perfect gas law, c_p is the lifting gas specific heat capacity at constant pressure, taken here as constant, and $\langle \cdot \rangle$ refers to the average over the balloon volume. Regarding the boundary

conditions, the lifting gas temperature at the balloon surface is assumed to be the same as the ambient air temperature, viz. $T_b(r=1) = T_a$. At the balloon center, the heat flux is imposed to vanish as a result of the symmetry of the problem, viz. $(\partial T_b / \partial r)_{r=0} = 0$.

Equation (4) presents a simplification, because the work and convection terms associated with the expansion of the gas are not considered. This avoids the requirement of using the mass conservation equation to close the system. It should be noted that the suppression of the expansion terms is equivalent to considering the gas as incompressible; in particular, it implies that the balloon effective radius remains constant while heat diffuses. This constraint is justified for the small time intervals (0.3–1 s, see Sect. 3) over which heat diffusion is evaluated using Eq. (4). At the end of each time interval, both the temperature distribution and the balloon effective radius are corrected to account for the gas expansion. The correction procedure will be described later in Sect. 3.

The molecular heat diffusion coefficient is approximated by its average over the balloon volume. This approximation constitutes a correction to the fact that heat convection is not taken into account in the present model. In addition, $\langle D \rangle$ is assumed to be constant over time intervals of a few seconds. This is granted because so short time intervals correspond to just a few percent of the characteristic time of diffusion (see discussion below). The assumption of constant $\langle D \rangle$ is particularly valuable since it turns Eq. (4) into a simple partial differential equation.

Under these conditions Eq. (4) is amenable to an analytical solution (Carslaw and Jaeger, 1959). The latter is expressed as a Fourier series whose coefficients involve the computation of integrals over the radial coordinate r , requiring significant computational effort. In the balloon ascent model, we rather solve Eq. (4) numerically by the Finite Element Method. For a description of the Finite Element Method applied to the problem of heat diffusion, see e.g. Lewis et al. (1996). The analytical solution is however useful in two different aspects. Firstly, it can be used to estimate the magnitude of the characteristic time of diffusion, $\tau = R^2 / (\pi^2 D)$. The estimate is calculated in Appendix A. It is found that τ decreases from ~ 900 s at ground to ~ 300 s at 30 km altitude, validating that the temperature distribution inside the balloon varies little over time intervals of a few seconds. Secondly, the analytical solution can be used to study the convergence of the finite element solution in simple cases of reference. Evidences for the convergence of the numerical solution are provided in Appendix B.

2.3 Balloon drag coefficient

In this section, the dynamics of the drag coefficient of a perfect sphere are detailed first. These are then used as a basis for the discussion of the drag coefficient of spheroids, aimed at illustrating the case of almost spherical objects. From these two steps, the current knowledge on the drag coefficient

of objects placed in a cross-flow is found to be insufficient to precisely model the balloon ascent. To compensate for this, information on the drag coefficient of sounding balloons is extracted from experimental flights in a third step.

2.3.1 Drag coefficient of a perfect sphere

As pointed out by numerous experimental studies (e.g., Son et al., 2010), the drag coefficient of a perfect sphere is mainly a function of two other dimensionless numbers, namely the Reynolds number, Re , and the free-stream turbulence intensity, Tu (see below). The Reynolds number is a measure of the ratio of inertial energy, $\rho_a v_z^2$, to viscous energy, $\mu v_z / R$, where μ is the dynamic viscosity of the fluid. Consequently, $Re = \rho_a R v_z / \mu$ quantifies the relative importance of these two types of energies for given flow conditions. In the case of a sounding balloon, whose typical effective radius is of the order of 1 m at ground and mean ascent rate of the order of 5 m s^{-1} , the Reynolds number decreases from $\sim 8\text{--}9 \times 10^5$ at ground to $\sim 6\text{--}9 \times 10^4$ at 30 km altitude. In this range of Reynolds numbers, the drag coefficient of perfect spheres undergoes a sudden increase, referred to as the *drag crisis*, as the Reynolds number decreases and experiences a transition from the super- to the sub-critical regimes (Vennard and Street, 1976). The drag crisis is explained by a transition of the boundary layer from turbulent to laminar as Re decreases, which advances the position of the boundary layer separation point upstream at the surface of the sphere (Vennard and Street, 1976). In summary, for a balloon ascending in the atmosphere the sequence of dynamical changes is as follows: height increases \rightarrow air density decreases $\rightarrow Re$ decreases \rightarrow boundary layer turns from turbulent to laminar \rightarrow boundary layer detachment point advanced upstream at the surface of the balloon \rightarrow drag coefficient increases. According to Achenbach (1972), the critical Reynolds number at which the drag crisis occurs, lies in the range $3.5\text{--}3.8 \times 10^5$ in the case of a negligible free-stream turbulence intensity ($Tu = 0.45\%$). His experimental curve obtained from a rigid sphere held fixed in space in a cross-flow wind tunnel is partly reproduced in Fig. 1. It can be observed that in the super-critical regime ($Re > 3.5 \times 10^5$) the drag coefficient slightly decreases from its starting value of ~ 0.1 at $Re = 10^6$, then rapidly increases during the drag crisis, before stabilizing in the sub-critical regime ($Re < 3.5 \times 10^5$) where it remains almost constant at a value of ~ 0.5 .

The free-stream turbulence intensity, Tu , is defined as the ratio of the standard deviation of the incident air velocity fluctuations to the mean incident air velocity (e.g., Son et al., 2010). Contrary to Re , Tu is purely a property of the fluid. As the free-stream turbulence intensity is increased, the critical Reynolds number is observed to shift to lower values (Son et al., 2010). This is explained by the turbulence intensity delaying the boundary layer transition from turbulent to laminar, hereby leading to a drag crisis at lower Reynolds numbers. The experimental drag curves of Son et al. (2010)

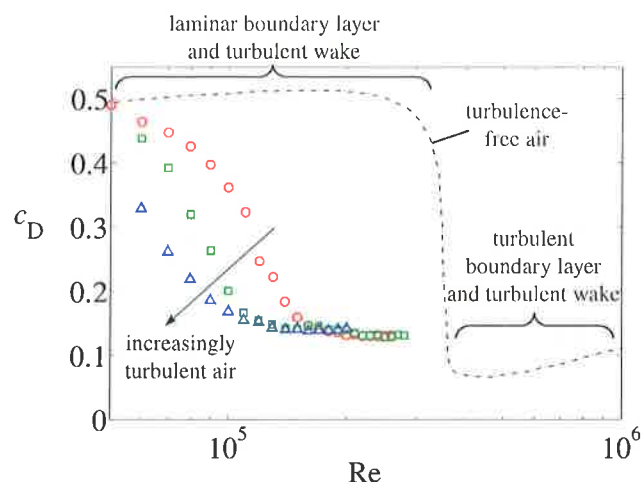


Fig. 1. Drag coefficient of a sphere as a function of the Reynolds number: $Tu = 0.45\%$ (---), data from Achenbach (1972); $Tu = 4\%$ (\circ), $Tu = 6\%$ (\square), $Tu = 8\%$ (\triangle), data from Son et al. (2010).

characteristic for a sphere held fixed in space at three different Tu values are also reproduced in Fig. 1, where the term “drag curve” refers to the curve of c_D as a function of Re at given Tu . It can be observed that a level of free-stream turbulence as low as 4%, which is a typical value of the turbulence intensity of the free troposphere (e.g., Hoyle et al., 2005), is sufficient to decrease the value of the critical Reynolds number by more than 50% as compared to the turbulence-free curve, leading to a decrease of c_D by as much as 70% in the range of Reynolds numbers $2\text{--}3 \times 10^5$. Likewise, the variation of c_D between the drag curves at $Tu = 4\%$ and $Tu = 6\%$ may reach more than 40% depending on the Reynolds number. It is concluded that the drag curve of a perfect sphere is extremely sensitive to the level of free-stream turbulence.

2.3.2 Drag coefficient of a spheroid

For a spheroid, the drag coefficient dependence on Re qualitatively resembles that of a perfect sphere as a result of the similarity of both shapes (Loth, 2008). In particular, also the drag coefficient of a spheroid is a function of Re and Tu . It is expected to tend to the value for a perfect sphere as the respective lengths of the principal axes of the spheroid converge to the same value. Thus, the drag coefficient of a spheroid also depends on the departure of the spheroid shape from a perfect sphere. This departure is measured in terms of the aspect ratio, E , defined as the ratio of the length of the vertical symmetry axis to that of the horizontal axes of the spheroid. For example, Loth (2008) reports that the drag coefficient of an oblate spheroid with $E = 0.5$ is about twice that of the volume-equivalent sphere for $2 \times 10^3 < Re < 3 \times 10^5$ and negligible Tu .

To the best of the authors’ knowledge, Eric Loth (2008) is the only author to report experimental investigations of the drag coefficient of spheroids at very high Reynolds numbers ($Re > 10^4$). He unfortunately considers only one single value for the aspect ratio, namely $E = 0.5$. He also does not investigate the influence of the free-stream turbulence intensity on the drag curve. More importantly, his study does not extend beyond $Re > 3 \times 10^5$, which leaves the entire supercritical regime unexplored to date. It should be noted that these last two limitations do not apply only to the work of Loth on the drag coefficient of spheroids, but also to all studies published to date on the drag coefficient of non-spherical objects. To compensate for this lack of knowledge, and since parameters other than Re , Tu and E – such as unsteadiness or turbulence intensity length scale – are also known to affect the drag coefficient (e.g. Wang et al., 2009; Neve, 1986), an attempt is made here to derive a mean experimental drag curve for sounding balloons, based on a dataset of balloon flights. This attempt is expected to resolve also another principal complication, namely the fact that experimental investigations of drag coefficients normally let a heavy body fall freely in a viscous fluid or hold a solid body fixed in space and then expose it to a flow of the surrounding medium, e.g. in a wind tunnel. In such experiments detaching vortices in the wake of the particle affect very little the motion of the body, whose mass, due to the setup, appears to be extremely high. In contrast, a sounding balloon, whose mass is only a small fraction of that of the displaced air, is severely affected by the detaching vortices. As such, the analysis of a dataset of observed ascents appears to be the best way forward at the present time.

2.3.3 Procedure for the derivation of a drag curve for sounding balloons from experimental flights

The dataset is chosen from the flights which took place at Lindenberg (Germany) in 2008 during the Lindenberg Upper Air Methods Intercomparisons (LUAMI) flight campaign, whose main aim was to compare different airborne water-vapor sounding methods (Immler, 2008). During the campaign, the masses of the payload (including the parachute) and the balloon envelope were measured before each flight, as well as the uplift mass; this allows for the balloon total mass, m_{tot} , and the balloon radius at ground, $R(z=0)$, to be calculated. It should be mentioned that the uplift mass is defined as the value of the payload mass for which the free lift is equal to zero (see Sect. 2.1). Respective uncertainty errors of ± 100 g and ± 200 g in the measurements of the uplift and payload masses cannot be excluded, which in turn result in respective uncertainties of ± 200 g and $\pm 10^{-2}$ m in m_{tot} and $R(z=0)$. During the flights, air temperature and pressure were measured every second by the radiosondes. The balloon altitude was also recorded at the same frequency by a GPS on board the radiosondes. Of the 27 balloons launched during the campaign, only the 15 released at night are kept in this analysis to enforce the assumption of negligible radiative

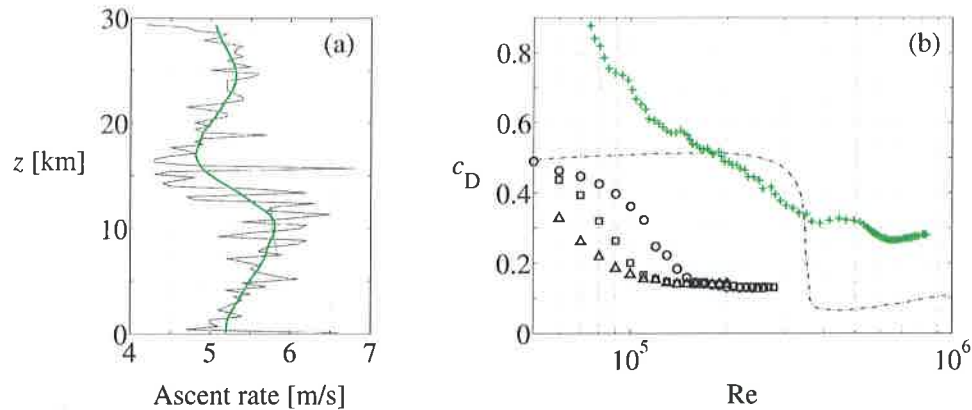


Fig. 2. Derivation of the experimental drag curve from LUAMI flight L007 launched on 7 November 2008 at 22:45 UTC. **(a)** The 60 s-low pass filtered ascent rate profile derived from the GPS data (—), and its mollified version using $\varepsilon = 4$ km (---); **(b)** experimental drag curve derived using the procedure described in Sect. 2.3 (+). The curves of Achenbach (1972) and Son et al. (2010) for a perfect sphere are reported here for comparison (see Fig. 1).

heat transport into the balloon. A further selection is made removing five flights, three presenting strong evidence of defect (error in the reported value of the measured uplift mass or in the recording of the flight data) and two using a different type of sounding balloon. The dataset is therefore left with ten flights in total, all of which used the same type of sounding balloon, namely the TX1200 balloon from the Japanese company Totex.²

In order to derive a drag curve for sounding balloons from each of the ten selected experimental flights, the drag coefficient is calculated from Eq. (3) every minute of each flight as a function of v_z , R and ρ_a . To this end, the balloon radius is computed using the algorithm presented in Sect. 3, and the air mass density is determined from the 60-s low pass filtered atmospheric temperature and pressure data recorded during the balloon ascent. The challenge lies in the estimation of v_z , as only the ascent rate with respect to the ground, $v_{z,g}$, can be deduced from the radiosonde GPS data. The ascent rate in still air corresponds to the vertical velocity measured with respect to ambient air, which cannot be directly retrieved from the measurements. Thus, only an estimate of v_z can be obtained by smoothing the profile of $v_{z,g}$ as a function of altitude. This procedure is based on the assumption of vertical air motion having a normal distribution with near-zero mean value (Wang et al., 2009). The smoothing process is performed by convoluting the vertical profile of $v_{z,g}$ with the mollifier $\eta_\varepsilon(z)$, where

$$\eta_\varepsilon(z) = \begin{cases} (c/\varepsilon) \exp[\varepsilon^2/(z^2 - \varepsilon^2)] & \text{if } z \in [-\varepsilon, \varepsilon], \\ 0 & \text{otherwise,} \end{cases} \quad (5)$$

and the constant c is chosen to ensure the unity of the integral of η_ε (Salsa, 2008). The parameter ε controls the spatial scale on which the profile of $v_{z,g}$ is smoothed. A value of $\varepsilon = 4$ km

is chosen here so as to ensure that gravity waves, whose typical vertical wavelengths are 2–5 km in the lower stratosphere (Fritts and Alexander, 2003), are properly removed from the measured ascent rate by the smoothing process. Other values ($\varepsilon = 2$ km and $\varepsilon = 5$ km) have been investigated, but with negligible influence on the derived experimental drag curve (not shown).

An example of balloon ascent rate profile and of its associated mollified version is shown in Fig. 2a. The profile is observed to present an overall S-shape, which is typical for sounding balloons and can be simply explained by Eq. (3). Due to the diffusion of heat inside the balloon, the difference between the mean balloon temperature and the atmospheric temperature remains approximately constant over the troposphere and the stratosphere separately (not shown). Under this condition, it can be shown that the expression of v_z in Eq. (3) is proportional to the $-1/6$ power of the atmospheric density (Yajima et al., 2009). This accounts for the fact that the balloon ascent rate increases with altitude over the troposphere and the stratosphere separately. The decrease in the ascent rate at the tropopause results from the sudden increase in the potential temperature. This can be interpreted as the balloon being suddenly colder than its environment and therefore decelerating, until its temperature difference with the surrounding atmosphere stabilizes and its ascent rate increases again as the $-1/6$ power of the atmospheric density. The decrease of the ascent rate above 25 km altitude observed in Fig. 2a is thought to result from another process. Shortly before bursting, the envelope of the balloon presents bubbles and excrescences on its surface due to an inhomogeneous distribution of the envelope material. This is expected to substantially increase the drag coefficient and consequently be at the origin of the balloon deceleration.

The drag curve corresponding to Fig. 2a and obtained by the aforementioned procedure is depicted in Fig. 2b. As

²<http://www.totex.jp>

expected from the aspherical shape of the balloon, this curve is observed to deviate significantly from those by Achenbach (1972) and Son et al. (2010) for a perfect sphere. However, the balloon drag curve presents a qualitative shape similar to the curves by Son et al. at $Tu = 6\%$ and $Tu = 8\%$. This suggests that the turbulence intensity of the atmosphere is of the order of 6% to 8%, which is in the range of typical values for the free troposphere reported by Hoyle et al. (2005). Comparison of the balloon drag curve with the curves by Son et al. reveals that the drag coefficient of the balloon is on average three times higher than the one of its volume-equivalent sphere. This difference cannot be solely explained by the asphericity of the balloon. Indeed, Loth (2008) reports an increase of only 100% in the drag coefficient of a spheroid with $E = 0.5$ as compared to a perfect sphere in the range of Reynolds number $0.5\text{--}3 \times 10^5$ and at negligible Tu . The magnitude of this increase is expected to remain of roughly the same order at $Tu > 0$, while reducing with higher values of E . Therefore, the increase in c_D due to the limited departure of the balloon shape from spherical is clearly less than a factor of 2. This leaves part of the observed discrepancy between the balloon's and the perfect sphere's drag curves unexplained. Mainly three mechanisms are thought to be responsible: the pendulum effect of both the parachute and the payload attached to the balloon (Wang et al., 2009), the deformation of the balloon shape through the propagation of waves on its elastic envelope and the generation of vorticity in the wake of the balloon.

Regarding the latter mechanism, Govardhan and Williamson (2005) report the observation of two vortex threads detaching periodically from behind spheres placed in a cross-flow. In their experiments, the spheres are attached with a single tether to the upper wall of the wind tunnel so as to let them free to move in the horizontal plane (in both the directions parallel and perpendicular to the flow). The authors elegantly demonstrate that the periodically detaching vortex threads exert an oscillating force on the spheres in a direction transverse to the flow. Yet, Veldhuis et al. (2009) demonstrate that this force is usually not restricted to the plane transverse to the flow in the case of buoyant spheres rising freely in a Newtonian fluid. As a consequence, the component of this force in the direction of the spheres' motion is non-zero, which results in a so-called *lift-induced* drag. The latter adds to the drag predicted from the curves by Achenbach (1972) or Son et al. (2010) for a sphere held fixed in space. Thus, Veldhuis et al. estimate the apparent c_D of spheres rising freely to be higher by a factor 1.5 to 2 than expected from the standard drag curves alone. Unfortunately, the range of Reynolds number they consider is limited to the interval $1\text{--}2 \times 10^3$. However, we expect the generation of a lift-induced drag to be significant also for higher values of Re , and even more so for buoyant objects with non-spherical shape. This may account for a significant fraction of the unexpected drag depicted in Fig. 2b.

From a physical point of view, the balloon drag curve pictured in Fig. 2b is supported by the specifications of the balloon manufacturing company, according to which the balloon drag coefficient at $Re \sim 5\text{--}8 \times 10^5$ is in the range 0.2–0.3. Furthermore, this curve is in good agreement with the observations of Mapleson (1954), who reports an increase of up to 400% in the drag coefficient of sounding balloons as compared to a perfect sphere for $1.3 \times 10^5 < Re < 7 \times 10^5$.

2.3.4 Reference drag curve for sounding balloons

The drag curves derived from the ten LUAMI flights all present the same qualitative behavior as the curve described above. However, there are systematic offsets in c_D amongst these ten drag curves in the range $\pm 25\%$, corresponding to ± 0.15 absolute units in c_D , as shown by the light gray curves in Fig. 3. We must attribute part of these offsets to errors in the estimated uplift and payload masses, i.e. in the preparatory measurements before each balloon launch during the LUAMI campaign. Indeed, an error of 100 g in the uplift mass shifts the corresponding drag curve by 6% through its effect on the values of $R(z=0)$ and m_{tot} (not shown). Similarly, an error of 200 g in the payload mass would result in a shift of 7% in the balloon drag curves. Therefore, such errors might explain about half of the observed offsets in c_D . The other half might be due to differences in the manufacturing process of the individual balloons, as invoked by Mapleson (1954) to explain the divergence of his results. While we cannot correct for these unknown differences in the manufacturing process, the confidence ranges of the uplift and payload masses can be taken into account in order to reduce the spread of the drag curves. To this end, $R(z=0)$ and m_{tot} are adjusted within their accepted confidence ranges, minimizing the mean-square difference between the drag curves. The ten drag curves with adjusted offsets are pictured in green in Fig. 3. They are then fitted by a second-order polynomial in order to retrieve the single reference drag curve (blue line), which will be used in Sect. 3 to derive the balloon ascent rate in still air:

$$c_D = 4.808 \times 10^{-2} (\ln Re)^2 - 1.406 \ln Re + 10.490. \quad (6)$$

The mean standard deviation of the ten experimental curves with respect to the polynomial fit is equal to 4.1×10^{-2} . Therefore, the values of the drag coefficient derived from the reference curve must be considered to have an uncertainty error of approximately ± 0.04 .

Several important aspects of Eq. (6) should be stressed. First, the expression of the drag coefficient is observed not to depend on the turbulence intensity of the atmosphere. This results directly from the impossibility to determine Tu to the necessary precision from balloon flights, and implies that Eq. (6) accounts only for the mean profile of the atmospheric turbulence intensity. Deviations from this mean profile, such as the generation of turbulence intensity through gravity wave breaking, cannot be taken into account by the

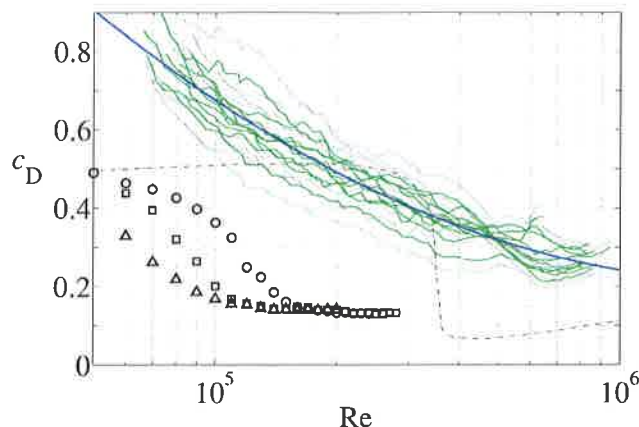


Fig. 3. Derivation of a reference drag curve for sounding balloons. (—) Experimental drag curves derived from the ten LUAMI balloon flights; (—) same but with adjusted values for $R(z=0)$ and m_{tot} ; (—) fit to the ten experimental drag curves using a second-order polynomial (Eq. 6). The curves of Achenbach (1972) (dashed) and Son et al. (2010) (symbols) for a perfect sphere are shown for comparison (see Fig. 1).

model. Second, Re in Eq. (6) is a function of the balloon ascent rate (see Sect. 2.3.1). As a consequence, fluctuations in the balloon vertical velocity are explicitly taken into account in our drag calculation. Finally, it should be emphasized that Eq. (6) is valid only for TX1200 balloons launched at night. However, the procedure described above could be applied to any set of soundings featuring the required data. We have for example derived a reference drag curve for the two TX2000 balloons launched at night during the LUAMI campaign, and which were removed from the original dataset of night flights in Sect. 2.3.3. As compared to the TX1200 balloons, the values of the drag coefficient have been observed to be lower in the troposphere and much higher in the stratosphere (not shown), hereby pointing to the significant impact of the balloon shape on the drag curve.

3 Balloon ascent model

The balloon ascent model developed in this work aims to determine the ascent rate of sounding balloons in still air as a function of time. The model's time step is denoted by Δt in the following and the corresponding increase in the balloon altitude by Δz ; the two are related through the relation $\Delta z = v_z \Delta t + O(\Delta t^2)$.

A single step of the model comprises two parts:

1. the computation of the balloon effective radius and radial temperature distribution at time $t + \Delta t$ knowing their values at time t ; and

2. the simultaneous determination of the drag coefficient and the balloon ascent rate in still air at time $t + \Delta t$ from Eq. (3).

For convenience of the reader, the computations performed in these two parts – to be detailed below – are summarized under the form of a pseudo-code in Fig. 4.

In order to increase the accuracy of the balloon's effective radius computation, part 1 uses substeps to resolve the balloon effective radius at intermediate times between t and $t + \Delta t$. The intermediate times are computed using a sub-time step, δt , chosen as a fixed fraction of the characteristic time of diffusion. This ensures that Eq. (4) is solved using a constant normalized time step, $\delta t/\tau$, during the whole balloon ascent. In the following discussion, let $\{t_n\}_{n=1,\dots,N}$ be the set of intermediate times between t and $t + \Delta t$, where $t_n = t + n\delta t$ and N is the number of intermediate steps. In a single substep of part 1, the balloon effective radius at time t_{n+1} is computed from the balloon effective radius at time t_n in three stages (see left panel of Fig. 4):

- (i) *Adiabatic expansion of the balloon* (pictured in Fig. 5a).

In this stage, the balloon is considered to ascend from altitude $z(t_n)$ to altitude $z(t_{n+1})$. Let R^* and T_b^* denote respectively the balloon effective radius and temperature distribution inside the balloon after the adiabatic expansion has taken place. Assuming that the pressure remains uniform inside the balloon and equilibrates with the ambient atmospheric pressure during the process,

$$R^* = \left(\frac{p_a(t_n)}{p_a(t_{n+1})} \right)^{1/3\gamma} R(t_n), \quad (7)$$

$$T_b^*(r) = \left(\frac{p_a(t_n)}{p_a(t_{n+1})} \right)^{(1-\gamma)/\gamma} T_b(r, t_n), \quad (8)$$

where $\gamma = c_V/c_p > 1$ is the adiabatic index of the lifting gas (c_V is the lifting gas specific heat at constant volume) and Eq. (8) is valid for all $r \in [0, 1]$. In the right-hand side of Eq. (8), r denotes the radial coordinate normalized by $R(t_n)$, whereas in the left-hand side it is normalized by R^* .

- (ii) *Heat diffusion inside the balloon at constant pressure* (pictured in Fig. 5b). As stated above in Sect. 2.2, this stage assumes the lifting gas to be incompressible; as a consequence, the balloon volume remains constant during the diffusion of heat. The mean heat diffusion coefficient is computed from the temperature distribution T_b^* obtained in stage (i). Assuming that $\langle D \rangle$ remains constant, Eq. (4) is then solved numerically by the Finite Element Method using a time step of $\delta t = t_{n+1} - t_n$. T_b^* is chosen as the initial temperature distribution, and the temperature at the balloon surface

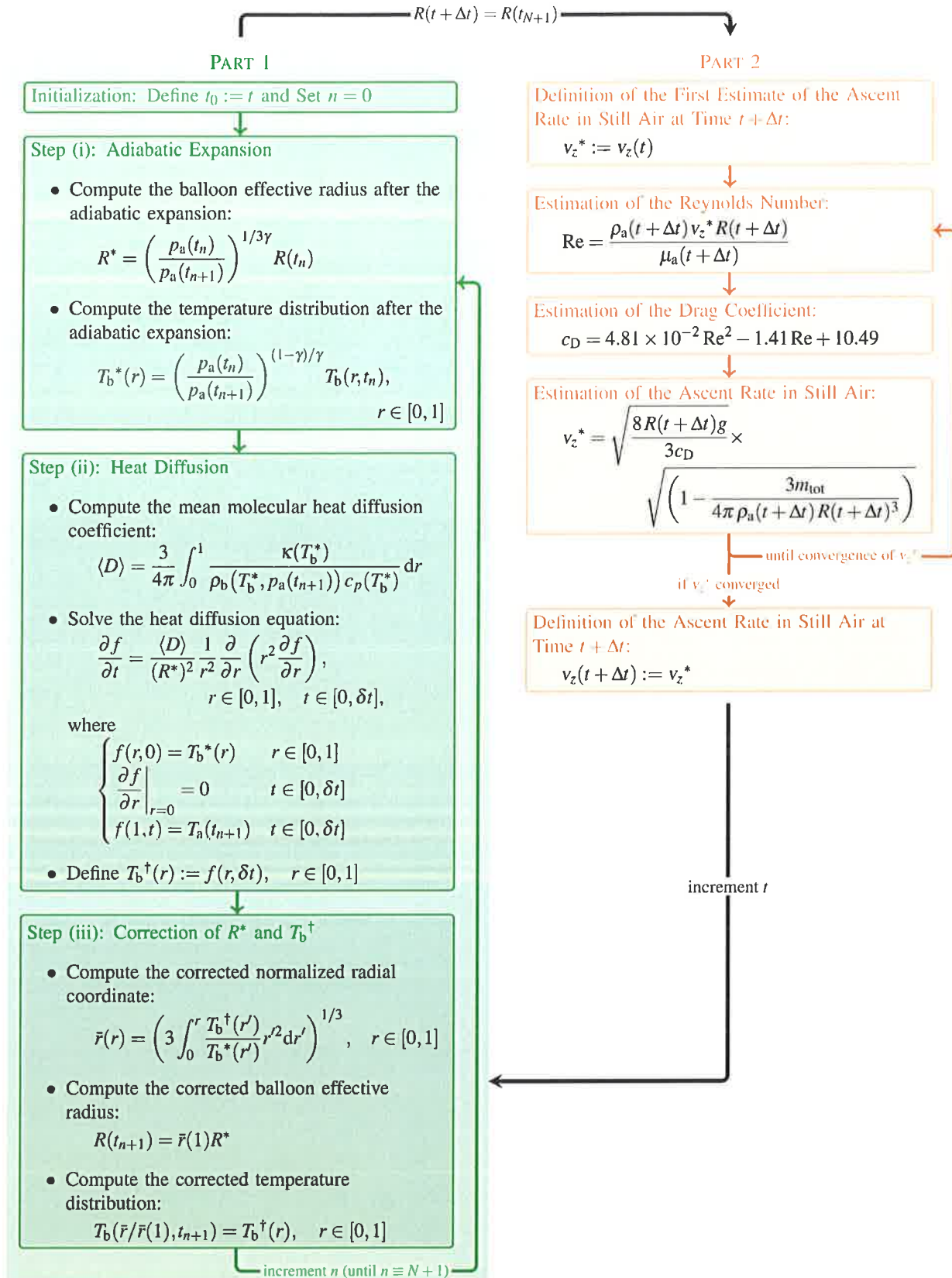


Fig. 4. Schematic representation of the different steps of the model. The notation is introduced in Sect. 3.

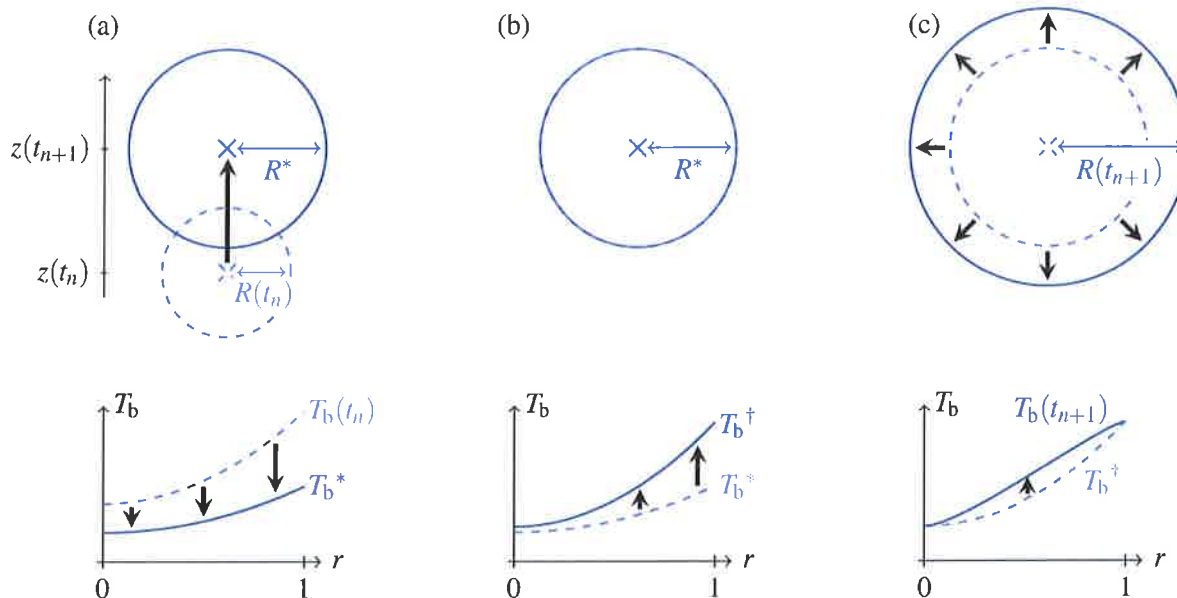


Fig. 5. Schematic representation of the three stages used in part 1 of the model to compute the balloon effective radius at time t_{n+1} from the balloon effective radius at time t_n . The upper panel shows the evolution of the balloon altitude and effective radius at each step, the lower panel indicates the corresponding changes in the temperature distribution inside the balloon. The notation used in the figure is introduced in Sect. 3. **(a)** Adiabatic expansion of the balloon from altitude $z(t_n)$ to altitude $z(t_{n+1})$. **(b)** Heat diffusion inside the balloon at constant pressure. **(c)** Correction to the balloon effective radius and temperature distribution.

is kept constant and equal to $T_a(t_{n+1})$. The temperature distribution at the end of the diffusion process is denoted by T_b^\dagger .

- (iii) *Correction to the temperature distribution and balloon effective radius (pictured in Fig. 5c).* To compensate for the above assumption of gas incompressibility during the diffusion of heat, T_b^\dagger and R^* are corrected in this stage. To this end, let S be a spherical shell concentric to the balloon and whose normalized radius and infinitesimal thickness are denoted by r ($r < 1$) and dr , respectively. The temperature of S is known from step (ii) to be $T_b^\dagger(r)$. Given this configuration, the aim is to find the normalized radius and thickness, respectively denoted by \bar{r} and $d\bar{r}$, that S would have had if it had been let expand in step (ii). In such a case, its temperature would still have increased from $T_b^*(r)$ to $T_b^\dagger(r)$ as a result of heat diffusion. On the other hand, its pressure would have remained constant and equal to $p_a(t_{n+1})$, while its volume would have increased from $4\pi r^2 dr$ to $4\pi \bar{r}^2 d\bar{r}$. Using the ideal gas law in association with the conservation of gas moles inside S ,

$$\frac{4\pi r^2 dr}{T_b^*(r)} = \frac{4\pi \bar{r}^2 d\bar{r}}{T_b^\dagger(r)}. \quad (9)$$

In this equation, \bar{r} is understood as a function of the uncorrected normalized radius r . Integrating Eq. (9) with

respect to r ,

$$\bar{r}(r) = \left(3 \int_0^r \frac{T_b^\dagger(r')}{T_b^*(r')} r'^2 dr' \right)^{1/3}. \quad (10)$$

It must be emphasized that both \bar{r} and r are normalized by the balloon effective radius R^* resulting from step (i). Thus, the corrected balloon effective radius at time t_{n+1} is given by

$$R(t_{n+1}) = \bar{r}(1) R^*, \quad (11)$$

and the corrected balloon temperature distribution at time t_{n+1} reads

$$T_b(\bar{r}/\bar{r}(1), t_{n+1}) = T_b^\dagger(r), \quad (12)$$

where $\bar{r}(1)$ is evaluated from Eq. (10).

Stages (i)–(iii) are repeated $N + 1$ times until the balloon effective radius at time $t + \Delta t$ is evaluated. This terminates part 1 of the model.

In part 2, Eq. (3) is used to compute the balloon ascent rate in still air at time $t + \Delta t$ (see right panel of Fig. 4). The required air mass density is determined from the ambient atmospheric temperature and pressure, and the result obtained in part 1 is used for the balloon effective radius. The drag coefficient is determined from the reference second-order polynomial drag curve shown in Fig. 3. To this end, an estimation

of the Reynolds number at time $t + \Delta t$ is derived from the balloon ascent rate at time t . The estimated Re is then reported in the drag curve to estimate the drag coefficient. By inserting the latter in Eq. (3), a first estimate of $v_z(t + \Delta t)$ is obtained, which is subsequently used to refine the initial estimate of Re . This generates a loop, which is iterated until the convergence criterion is satisfied, namely until the relative variation of the ascent rate between two successive loops is less than $5 \times 10^{-4} \%$. At the end of part 2 of the model, the values of both c_D and v_z at time $t + \Delta t$ are known.

The vertical profile of the balloon ascent rate in still air is derived by going through parts 1 and 2 of the model at each time step. The value of Δt is fixed here to 1 min, which corresponds to a vertical resolution of ~ 300 m. Based on a trade-off between computational time and the convergence study presented in Appendix B, the choice $\delta t = 10^{-3} \tau$ is made, τ being computed at each step of the model. This results in a number of substeps (N) increasing from ~ 60 to ~ 180 between ground level and 30 km altitude.

To reflect the uncertainty in the reference drag curve (see end of Sect. 2.3), three different runs of the model are recommended. The first run, corresponding to the reference case, uses the reference drag curve itself to calculate the most probable profile of the balloon ascent rate in still air. The two additional runs are aimed at determining the range of uncertainty in this profile. To this end, they are based on instances of the reference drag curve shifted along the c_D -axis by $-\sigma_{c_D}$ and $+\sigma_{c_D}$, respectively, where $\sigma_{c_D} = 0.04$ denotes the uncertainty in the values of the drag coefficient derived from the reference drag curve (see Sect. 2.3).

In case the model is run *after* the balloon flight, advantage can be taken of the data collected during the ascent to improve the model in two respects. Firstly, the ascent rate derived from the GPS data can be used to correct the reference drag curve. The procedure consists in shifting the latter along the c_D -axis so as to minimize the mean-square difference between the measured and modeled ascent rate profiles. This process is based on the assumption that the vertical wind follows a normal distribution with near-zero mean value, as supposed by Wang et al. (2009). Secondly, the uncertainty in the values of the drag coefficient derived from the shifted reference drag curve can be narrowed down. This uncertainty has been estimated for the general case in Sect. 2.3, where it has been defined as the mean standard deviation, σ_{c_D} , of the difference between the experimental drag curves and the reference drag curve. In case the model is run after the actual flight, the experimental drag curve associated with the flight can be computed following the procedure described in Sect. 2.3. Only this experimental curve – instead of the ten of Fig. 3 – is then used to estimate the uncertainty in the values of c_D derived from the shifted reference drag curve. This uncertainty, denoted by $\sigma_{c_D}^*$, corresponds to the standard deviation of the difference between the experimental drag curve associated to the flight and the shifted reference drag curve. It is observed that $\sigma_{c_D}^*$ is generally lower as compared to σ_{c_D} .

4 Model evaluation and potential application

4.1 Model evaluation

Due to the lack of available flight data with precisely measured uplift and payload masses, the validating set considered in this section is composed of the same ten LUAMI night flights used in Sect. 2.3 to derive the reference drag curve. Following the procedure described in the previous section, the latter is corrected for each flight so as to minimize the departure of the modeled ascent rate from the measured one. It should be noted that this section does not consider the payload and uplift masses measured before each flight during the LUAMI campaign, but rather the adapted values of these masses calculated in Sect. 2.3 to reduce the spread in the experimental curves.

An example of adapted drag curve is pictured in Fig. 6a; the corresponding profile of the balloon ascent rate in still air is shown in Fig. 6b. In this case, the correction of the reference drag curve allows for the decrease of the discrepancy between the modeled and measured ascent rates by $\sim 0.4 \text{ m s}^{-1}$ below 10 km altitude. On the other hand, the balloon ascent rate in still air derived from the corrected reference drag curve appears to be overestimated in some regions, mostly in the lower troposphere below 2 km altitude and just below the tropopause between 10 and 12 km altitude. In these two altitude intervals, the Reynolds number is $7.5\text{--}8.5 \times 10^5$ and $4\text{--}5 \times 10^5$, respectively. As such, the apparent over-estimations of the ascent rate are related to the local maxima of the experimental drag curve at $Re = 8.5 \times 10^5$ and $Re = 4 \times 10^5$, respectively, which are unaccounted for by the (corrected) reference drag curve (see Fig. 6a). The latter considers lower drag coefficient values than the experimental drag curve at these Reynolds numbers, hereby leading to a lower drag force and consequently to a larger ascent rate in still air than expected from the smoothed observations. It must be emphasized that these apparent over-estimations of the ascent rate in still air may actually result from a local downward air motion affecting both the measured ascent rate and the experimental drag curve. Such a downdraft of the air would indeed slow down the actual ascent of the balloon and consequently increase its apparent drag coefficient, which could explain the observed difference between the reference and experimental drag curves. This could particularly be the case between 10 km and 12 km altitude, where the measured ascent rate is observed to drop below the lower uncertainty limit of the modeled ascent rate, hereby indicating a probable downward air motion. On the contrary, it is more likely that the overestimation of the ascent rate below 2 km altitude is due to the inaccuracy of the (corrected) reference drag curve. It should be mentioned that the presence of an unwinder between the balloon and its payload during the actual flight can be held responsible for part of the overestimation by the model. The unwinder – whose role is to progressively increase the length of the cable linking the payload

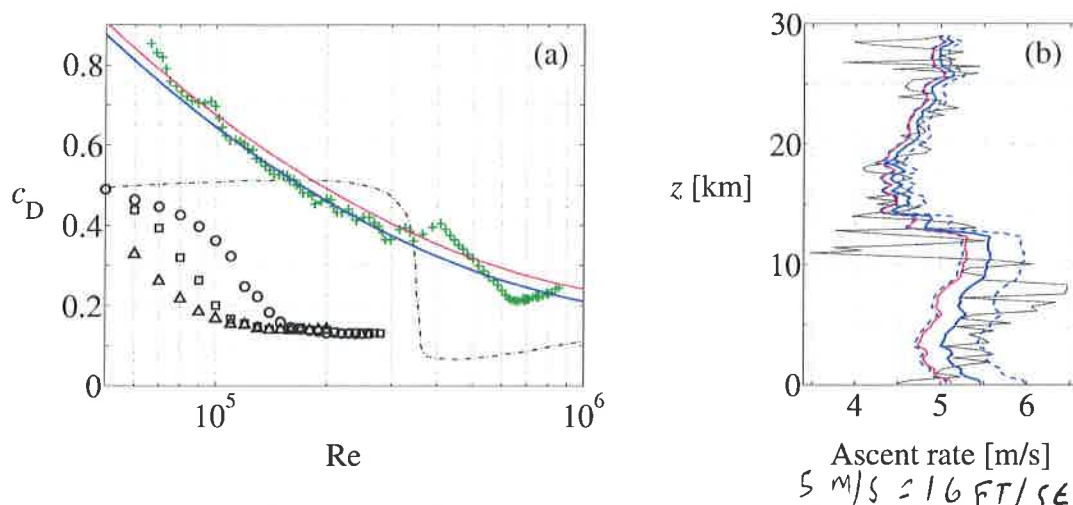


Fig. 6. Evaluation of the model on LUAMI flight L003b launched on 5 November 2008 at 22:45 UTC. **(a)** Corrected reference drag curve (—) obtained by shifting the reference drag curve (—, see Fig. 3) by -0.03 along the c_D -axis. The experimental drag curve derived from the flight is indicated by the green crosses. The curves by Achenbach (1972) and Son et al. (2010) for a perfect sphere are reported here for comparison (see Fig. 1). **(b)** Vertical profile of the balloon ascent rate in still air derived from the corrected drag curve (—), and the lower and upper limits of its range of uncertainty (---). The ascent rate in still air derived from the non-corrected reference drag curve (solid purple curve in panel (a)) is indicated here for comparison (—), along with the 60 s-low pass filtered ascent rate calculated from the GPS data (—).

to the balloon – remains active during the first 60 to 120 s of flight. Since the final length of the cable is about 50 m, this implies that the unwinder reduces the ascent rate of the payload as compared to that of balloon by 0.5 to 1 m s^{-1} in the lowermost 300 to 600 m of the ascent, which explains the lowermost part of the discrepancy between the modeled and the measured vertical velocities. No sharp conclusion can however be drawn regarding the precision of the model since the air vertical velocity was not measured independently during the LUAMI campaign.

The range of uncertainty in the ascent rate profile is obtained from the two additional runs of the model based on the reference drag curve shifted by $+\sigma_{c_D}^*$ and $-\sigma_{c_D}^*$ along the c_D -axis, respectively, where $\sigma_{c_D}^*$ denotes the standard deviation of the difference between the corrected reference drag curve and the experimental drag curve (see end of Sect. 3). In the case of the example pictured in Fig. 6, $\sigma_{c_D}^* = 0.03$. The corresponding uncertainty in v_z is shown in panel (b) of the figure; it is observed to decrease significantly when crossing the tropopause ($z = 12 \text{ km}$) while remaining globally constant over the troposphere and the stratosphere separately. This suggests the use of two different uncertainty ranges, the first one associated with the troposphere and the second one with the stratosphere. Averaging the uncertainty in v_z below and above the tropopause, respectively, it is found that the balloon ascent rate in still air is defined up to an additive factor of $\pm 0.4 \text{ m s}^{-1}$ in the troposphere, while this factor reduces to $\pm 0.2 \text{ m s}^{-1}$ in the stratosphere. The uncertainty error in v_z therefore decreases by a factor of ~ 2 when crossing the tropopause.

Evaluation of the model on the nine remaining LUAMI flights results in observations similar to those described above. The uncertainty in the modeled ascent rate averaged over the whole dataset is $\sim 0.5 \text{ m s}^{-1}$ in the troposphere and $\sim 0.2 \text{ m s}^{-1}$ in the stratosphere. As a consequence, it is assumed that the present model calculates the balloon ascent rate in still air with uncertainties of $\pm 0.5 \text{ m s}^{-1}$ and $\pm 0.2 \text{ m s}^{-1}$ below and above the tropopause, respectively, in the case where the flight data can be used to correct the reference drag curve. In comparison, Wang et al. (2009) model the balloon ascent rate in still air with an uncertainty of $\pm 0.9 \text{ m s}^{-1}$. On top of its increased accuracy, the present model enables the fairly good derivation of the ascent rate below 5 km altitude, contrary to the model by Wang et al. which systematically underestimates the ascent rate in this altitude range. As an example, a comparison of the two models on a particular flight is pictured in Fig. 7a. The present model is observed to be in greater agreement with the smoothed observations, particularly in the troposphere ($z < 12 \text{ km}$). This results in the altitude of the balloon as a function of time being modeled more accurately, as shown in Fig. 7b.

In the case where the flight data are not available to correct the reference drag curve (e.g. in forecasting applications), the uncertainty in the latter is higher; in particular, its associated values of the drag coefficient are determined up to a precision of $\pm \sigma_{c_D} = \pm 0.04$ (see Sect. 2.3). Similarly to above, the corresponding uncertainty in the modeled ascent rate is obtained by computing the difference between the profile derived by the first run of the model and the two additional profiles based on the reference drag curve shifted by $+\sigma_{c_D}$ and $-\sigma_{c_D}$ along the c_D -axis, respectively. The average

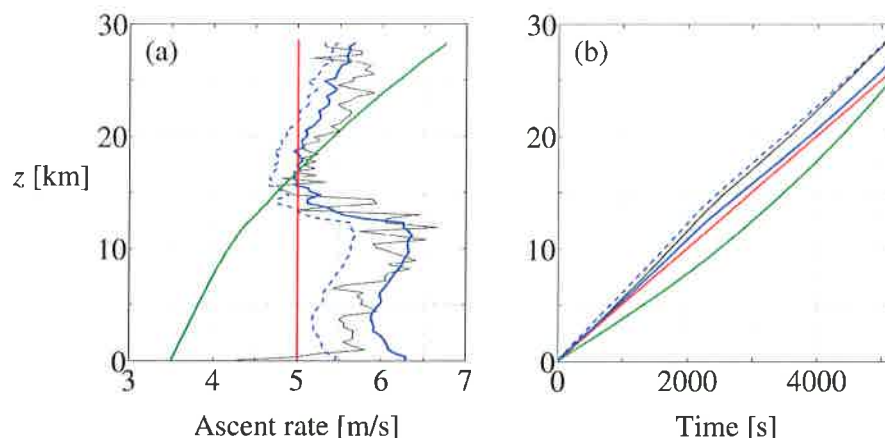


Fig. 7. Comparison of the predictions by different models with data measured during the balloon ascent in the case of LUAMI flight L005 launched on 6 November 2008 at 22:45 UTC. Measured data (—); predictions by the present model based either on the shifted reference drag curve (—) or on the reference drag curve itself (---); predictions by the model by Wang et al. (2009) (—); predictions by the model by Engel (2009) (—). **(a)** Vertical profile of the balloon ascent rate. **(b)** Altitude of the balloon as a function of time.

over the ten LUAMI flights estimates the uncertainty in the modeled ascent rate to be $\pm 0.6 \text{ m s}^{-1}$ in the troposphere and $\pm 0.3 \text{ m s}^{-1}$ in the stratosphere in this case. These uncertainty ranges are slightly larger than in the case where the reference drag curve can be corrected; they however remain smaller than those of the model by Wang et al. (2009). As pictured in Fig. 7a, the absence of correction to the reference drag curve may result in a systematic offset of the most probable ascent rate derived from the first run of the model as compared to the measured ascent rate. This is thought to result from differences in the manufacturing process of the individual balloons, responsible for an unpredictable variation of the drag coefficient from one balloon to the other, as mentioned previously in Sect. 2.3. In practice, this implies that the present model may systematically over or underestimate the balloon altitude as a function of time when used to forecast the balloon trajectory, as can be observed for example in Fig. 7b. The magnitude of the systematic error in the modeled ascent rate is bounded by the aforementioned limit of the uncertainty in v_z , namely 0.6 m s^{-1} in the troposphere and 0.3 m s^{-1} in the stratosphere. It should be mentioned that the current accuracy of the drag coefficient is closely linked to the LUAMI flight data set used for the derivation of the drag curve. Extending this analysis to more soundings with carefully recorded payload and uplift masses is therefore highly desirable.

The present model based on the (non-corrected) reference drag curve proves a better forecasting tool than the one by Engel (2009), which assumes for simplicity a constant ascent rate of 5 m s^{-1} . As a matter of fact, the error in the calculated balloon altitude at burst time, averaged over the ten LUAMI flights, is 1.4 km when using the present model as opposed to 2.7 km when using the model by Engel (not shown). The predictions of the two models can be compared on the par-

ticular example of Fig. 7a. It is observed that, despite its systematic offset, the present model based on the reference drag curve matches more precisely the overall profile of the measured ascent rate. This results in the altitude of the balloon as a function of time being forecasted more accurately by the present model, as shown in Fig. 7b.

4.2 Derivation of the vertical air motion

Given the above evidence for the model accuracy, the present section aims at illustrating an application: vertical air motion is estimated from the data collected during LUAMI flight L003a launched on 11 November, at 22:45 UTC. To this end, the balloon ascent rate in still air is calculated according to the model and then subtracted from the measured balloon ascent rate, as pictured in Fig. 8. The resulting profile of the air vertical velocity shown in panel (b) is difficult to validate owing to the same limitation as already encountered by Wang et al. (2009), namely the “lack of coincident [vertical velocity] data from other measurements.” In an attempt at compensating for this lack, the potential temperature lapse rate measured during the flight is taken as an approximate proxy for the vertical velocity. Indeed, in a first approximation, air parcels advected upwards cool down adiabatically on small spatial scales. As a consequence, their potential temperature, θ_a , remains approximately constant on such scales. We therefore expect the vertical profile of the potential temperature lapse rate, $d\theta_a/dz$, to present sharp decreases in regions of vertical updraft. Conversely, we expect the potential temperature lapse rate to increase significantly in regions of vertical downdraft, where air parcels of higher altitude and with larger potential temperature are advected downwards. Thus, in a first approximation, the profiles of the estimated vertical velocity of air and the potential temperature lapse rate should

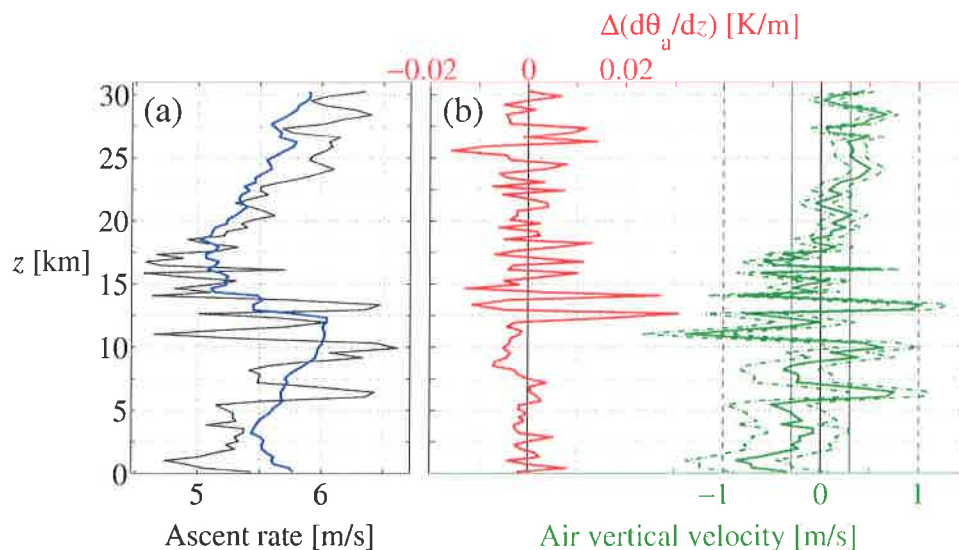


Fig. 8. Air vertical velocity during LUAMI flight L003a launched on 5 November 2008 at 22:45 UTC. **(a)** Balloon ascent rate in still air as calculated from the model (—); actual balloon ascent rate derived from the GPS data (—). **(b)** Air vertical velocity obtained by subtracting the ascent rate in still air from the actual ascent rate (—), and the upper and lower limits of its associated range of uncertainty (---); deviations of the potential temperature lapse rate from its still air value, derived from the atmospheric temperature recorded during the balloon ascent (—). The vertical velocities derived by Hoyle et al. (2005) from aircraft measurements are indicated here as thin gray lines for comparison: typical gravity-wave fluctuations, $\pm 0.3 \text{ m s}^{-1}$ (—); strong fluctuations representing less than $\sim 2\%$ of all wave occurrences, $\pm 1 \text{ m s}^{-1}$ (---).

present evidences of anti-correlation. This reasoning is nevertheless limited, since temperature fluctuations can be sensitive to both low- and high-frequency gravity waves, whereas vertical velocity fluctuations are more affected by higher-frequency gravity waves (Lane et al., 2003; Geller and Gong, 2010). As such, Gong and Geller (2010) experimentally observe that “the apparent dominant vertical wavelengths [of the gravity waves] estimated from T' [(temperature fluctuations)] and w' [(vertical velocity fluctuations)] profiles are different for some cases.”

Evidences of anti-correlation are however apparent on Fig. 8b, which pictures the vertical profile of $\Delta(d\theta_a/dz)$ beside the estimated profile of the air vertical velocity. The quantity $\Delta(d\theta_a/dz)$ corresponds here to the potential temperature lapse rate from which its mean value over the troposphere or stratosphere, depending on the altitude at which it is evaluated, has been subtracted. A particularly noticeable example of anti-correlation can be found in the altitude range 12–15 km, where the fluctuation amplitudes of the air vertical velocity and of the potential temperature lapse rate are relatively large. The correlation coefficient between the two profiles is -0.31 , and the probability that this value could be obtained at random from two independent distributions is as low as 2.4×10^{-3} . This suggests that the profiles of the air vertical velocity and of $\Delta(d\theta_a/dz)$ are globally anti-correlated.

However, the sole comparison with the potential temperature lapse rate does not enable us to validate the estimated

vertical air motion owing to the aforementioned limitations. This comparison also does not provide any quantitative information on the precision of the derived air vertical velocity. The analysis of the model uncertainty in the previous section however suggests that the uncertainty error of this velocity is within the range $\pm 0.5 \text{ m s}^{-1}$ in the troposphere and $\pm 0.2 \text{ m s}^{-1}$ in the stratosphere, as indicated in panel (b) of Fig. 8. Moreover, the estimated velocity is within the range of the typical vertical wind fluctuations in the troposphere reported by Hoyle et al. (2005) and indicated as thin gray lines in Fig. 8b. These fluctuations were derived from aircraft measurements performed during the SUCCESS campaign (Subsonic Aircraft: Contrail and Cloud Effects Special Study) which took place in the middle troposphere in cirrus clouds over the eastern Pacific Ocean. In their derivations, Hoyle et al. (2005) made sure to avoid perturbed regions to focus on free tropospheric gravity waves, similar to the situation during the LUAMI campaign in the northern German flatland.

One may argue that the vertical air motion could be estimated by a much more simplistic approach than the one presented above. Indeed, to obtain an approximation of the balloon ascent rate in still air, one may simply consider the smoothed profile of the actual balloon ascent rate (see Sect. 2.3) instead of using the balloon ascent model. A comparison of this simplistic approach with the one based on the model is shown in Fig. 9 in the case of LUAMI flight L025. The respective profiles of the balloon ascent rate in still air

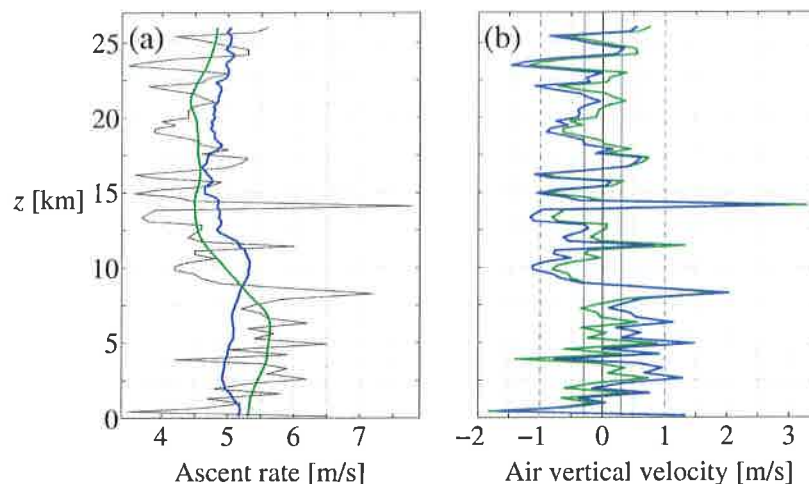


Fig. 9. Comparison of the model with the method based on the smoothing of the measured balloon ascent rate in the case of LUAMI flight L025 launched on 19 November 2008 at 22:45 UTC. **(a)** Vertical profile of the balloon ascent rate in still air derived from the model (—); smoothed profile of the balloon ascent rate measured during the actual flight (—) (for a description of the smoothing technique, see Sect. 2.3). The actual ascent rate derived from the GPS data is indicated as a thin black line for comparison. **(b)** Corresponding profiles of the air vertical velocity estimated from the model (—) and from the smoothed profile of the measured balloon ascent rate (—). The vertical velocities derived by Hoyle et al. (2005) from aircraft measurements are indicated here as thin gray lines for comparison: typical gravity-wave fluctuations, $\pm 0.3 \text{ m s}^{-1}$ (—); strong fluctuations representing less than $\sim 2\%$ of all wave occurrences, $\pm 1 \text{ m s}^{-1}$ (—).

estimated by the two methods are relatively dissimilar (see panel (a)). The one derived from the method using the model presents a finer resolution: it responds more physically to the fluctuations of the atmospheric temperature. In panel (b) of Fig. 9, it can be observed that the respective estimations of the air vertical velocity by the two methods differ by up to 0.5 m s^{-1} either in the troposphere and in the stratosphere. Yet, the method based on the model cannot be proven to describe the balloon ascent more precisely than the other one. The absence of independent measurements of the vertical air motion during the LUAMI campaign make the quantitative evaluation of any of the two approaches impossible.

5 Discussion and conclusion

Very few models of the ascent of sounding balloons in the atmosphere are available to date (Engel, 2009; Wang et al., 2009). In this study, a new model is proposed and shown to be an improvement over the present state of the art. Derived by equating the free lift and the drag force, the balloon ascent rate in still air is found to depend on three variables: the air mass density, the balloon drag coefficient and the balloon effective radius. The air mass density is assumed to be known either from numerical weather forecast or from the atmospheric temperature and pressure measured during the flight. The balloon effective radius, defined as the radius of the balloon's volume-equivalent sphere, is computed at each step of the model in three stages: (i) the balloon is first adiabatically expanded; (ii) heat is then allowed to diffuse at con-

stant pressure from the surrounding air into the balloon while assuming the lifting gas to be incompressible; and (iii) the effective radius and temperature distribution of the balloon are finally corrected to account for the expansion of the lifting gas discarded in step (ii). Since solar radiation – which has a strong impact on the balloon temperature distribution – is not resolved, the model is only applicable to night flights in its present state. Application to daytime soundings calls for a further study, but it should be possible provided that solar radiation is modeled as a diffusive process inside the balloon and that heating of the balloon envelope is taken into account. To compensate for the lack of data on the drag coefficient of almost spherical objects in a turbulent medium, a reference drag curve for sounding balloons is derived from a dataset of flights launched during the LUAMI campaign. This drag curve applies only to a particular type of sounding balloon, but using the methods we describe in this paper, it should be straightforward to derive a similar curve for other types of balloon. At each step of the model, the balloon drag coefficient can be obtained from the reference drag curve by refining the initial estimate of the Reynolds number through a loop.

A priori, the ascent rate in still air predicted by the model has an uncertainty of $\pm 0.6 \text{ m s}^{-1}$ in the troposphere and $\pm 0.3 \text{ m s}^{-1}$ in the stratosphere, where the range of uncertainty is defined as a difference of plus or minus one standard deviation from the calculated value. For some flights, a systematic offset between the predictions of the model and the subsequently measured actual ascent rate points to differences in the manufacturing process of the individual

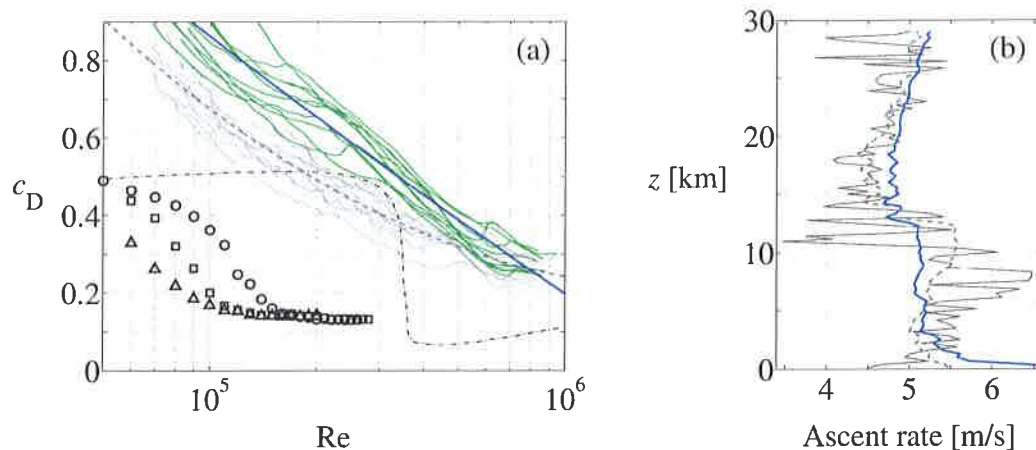


Fig. 10. Effect of the ten-fold increase of the mean molecular heat diffusion coefficient on the model. **(a)** Experimental drag curves derived from the ten LUAMI flights (—), and their associated reference drag curve (—), in the case of the enhanced $\langle D \rangle$. The ten experimental curves (—) and the reference drag curve (—) pictured in Fig. 3 are reported here for comparison, along with the curves by Achenbach (1972) and Son et al. (2010) for a perfect sphere. **(b)** Vertical profile of the balloon ascent rate in still air calculated from the corrected reference drag curve in the case of LUAMI flight L003b (see Fig. 6); $\langle D \rangle$ increased by a factor of ten (—); $\langle D \rangle$ normal (—). The 60-s low pass filtered vertical profile of the ascent rate calculated from the GPS data is indicated here for comparison (—).

balloons. These differences are responsible for unpredictable departures of the balloon drag coefficient from the reference drag curve and result in a mean uncertainty error of ± 1.5 km in the altitude of the balloon at burst time predicted by the model. The curve of the ascent rate in still air as a function of altitude captures the measured ascent rate profile very well, suggesting the model to be a valuable a priori trajectory forecast tool. As such, the algorithm could be used, for example, to improve the precision of the balloon trajectory forecasts required during match flight campaigns. Up to the present, forecast trajectory models used during such campaigns have assumed a constant ascent rate of 5 m s^{-1} for the balloon (e.g. Engel, 2009).

A posteriori, the data collected during the ascent can be used to adapt the reference drag curve and hereby reduce the discrepancy between the modeled and measured ascent rate profiles, as described in the final paragraph of Sect. 3. In this case, the air vertical velocity can be evaluated by subtracting the ascent rate in still air from the actual ascent rate. This procedure is shown to provide an estimation of the air motion which is within the range of the typical air velocity fluctuations derived by Hoyle et al. (2005) from the SUCCESS campaign in the middle troposphere (see panel (b) of Figs. 8 and 9). Its uncertainty error is estimated to be 0.5 m s^{-1} in the troposphere and 0.2 m s^{-1} in the stratosphere. In case this uncertainty could be reduced, the air vertical velocity derived in this way would be useful, for example to parametrize the cooling rate in cirrus cloud box models (Hoyle et al., 2005).

The neglect of heat eddy diffusion or heat convection inside the balloon affects the reference drag curve and the accuracy of the model. Indeed, assuming eddy diffusion or convection leads to an enhanced transfer of heat into the balloon

and therefore to an increase of the expansion of the balloon volume with altitude. As a consequence, the uplift force is larger mainly in the stratosphere, where the influence of the heat transfer into the balloon on the ascent rate is the strongest. This results – mainly in the region corresponding to the stratosphere ($5 \times 10^4 \leq Re \leq 5 \times 10^5$) – in the increase of the experimental drag curves derived from the ten LUAMI flights, as pictured in Fig. 10a, where $\langle D \rangle$ has been increased by a factor of ten in order to simulate eddy diffusion. As observed in the figure, the reference drag curve is steeper and shifted upwards in the case where eddy diffusion is resolved as compared to the case where only molecular diffusion is assumed. Based on this curve and the molecular heat diffusion coefficient increased ten times, the model is found to not capture the general feature of the ascent rate profile and particularly the maximum close to the tropopause. This appears clearly in the example pictured in panel (b) of Fig. 10, where the vertical profiles of v_z obtained from the model based on $\langle D \rangle$ and $10\langle D \rangle$, respectively, can be compared. This suggests that heat eddy diffusion and heat convection are not likely and that the main process responsible for the propagation of heat inside the balloon is molecular diffusion.

The model can be improved with respect to several aspects. Firstly, more experimental night flights should be used for the derivation of the reference drag curve, also during other seasons and in other locations. This would give the statistical mean performed by the polynomial fit more relevance from an ensemble point of view. Only ten flights are considered in this study owing for the plain difficulty to find high resolution datasets including accurate measurements of the uplift and payload masses. Indeed, as already noted by Wang et al. (2009), the uplift and payload masses

are currently neither measured precisely nor stored systematically before each flight. In fact, the information regarding these masses could be found only in the case of the balloons launched during the LUAMI campaign. Unfortunately, even during the LUAMI campaign it was not considered that mass measurements of great precision would be required later, which explains a part of the spread of the experimental drag curves discussed in Sect. 2.3. We therefore strongly suggest that the balloon launch protocols must take account of precise measurements and recordings of both the payload and uplift masses. Secondly, radiative heat transfer into the balloon could be resolved, which would allow for day flights to be modeled. Taking solar radiation into account would require the balloon envelope emissivity and the cloud cover to be considered, which would substantially complicate the treatment of heat inside the balloon. Finally, the validation of the reference drag curve lacks the support of studies on the drag coefficient of sounding balloons. In particular, the mechanisms at the origin of the large magnitude of this drag coefficient should be investigated in more detail. This includes an analysis of the deformation of the balloon shape during the ascent and a better characterization of both the lift-induced drag and the drag coefficient of almost spherical objects at very high Reynolds numbers and non-negligible turbulence intensity levels. Independent measurements of the air vertical velocity would also be useful for the validation of the reference drag curve.

Appendix A

Derivation of the characteristic time of diffusion

The analytical solution to Eq. (4) provided with the boundary conditions $T_b(1, t) = T_a(t)$ and $(\partial T_b / \partial r)_{r=0} = 0$ for all $t > 0$ reads (Carslaw and Jaeger, 1959):

$$T_b(r, t) = \frac{2}{r} \sum_{n=1}^{\infty} (\alpha_n + \beta_n(t)) e^{-D(\pi n/R)^2 t} \sin(\pi n r), \quad (\text{A1})$$

where

$$\alpha_n = \int_0^1 r T_{b,0}(r) \sin(\pi n r) dr,$$

$$\beta_n(t) = \frac{\pi D}{R^2} n(-1)^{n+1} \int_0^t T_a(s) e^{D(\pi n/R)^2 s} ds,$$

and $T_{b,0} : [0, 1] \mapsto \mathbb{R}$ denotes the initial temperature distribution. In Eq. (A1), $r \in [0, 1]$ and $t \geq 0$. The solution adopts a much simpler expression in the case where the initial temperature distribution is uniform, viz. $T_{b,0}$ is a constant, and the temperature at $r = 1$ is kept constant over time, viz. T_a is constant. In such a case,

$$\frac{T_a - T_b(r, t)}{T_a - T_{b,0}} = \frac{2}{\pi r} \sum_{n=1}^{\infty} \frac{(-1)^{n+1}}{n} e^{-D(\pi n/R)^2 t} \sin(\pi n r), \quad (\text{A2})$$

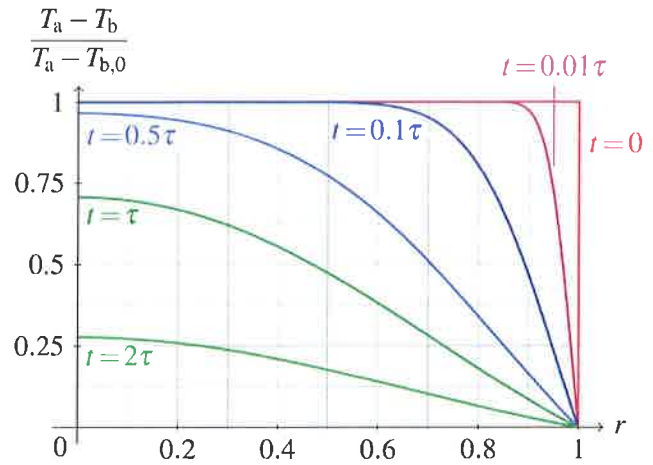


Fig. A1. Radial distribution of the quantity on the left-hand side of Eq. (A2) at different times. $\tau = R^2/(\pi^2 D)$ denotes the characteristic time of diffusion.

Table A1. Typical values of some parameters associated with the balloon at two different altitudes. The lifting gas is assumed to be hydrogen, whose specific heat capacity at constant pressure equals $1.4 \times 10^5 \text{ J kg}^{-1} \text{ K}^{-1}$.

Altitude	R (m)	κ ($\text{W m}^{-1} \text{ K}^{-1}$)	ρ_b (kg m^{-3})
ground	1	0.18	0.09
30 km	4	0.14	10^{-3}

where the quantity on the left-hand side is the temperature difference between the outside and the inside of the balloon normalized by the initial difference. The radial profile of this quantity is shown in Fig. A1 for different times. The characteristic time of diffusion is obtained from Eq. (A2) by considering only the dominant coefficient associated to $n = 1$ in the Fourier series, which leads to $\tau = R^2/(\pi^2 D)$. Using the expression $D = \kappa/(\rho_b c_p)$ and the typical values of Table A1, the characteristic time of diffusion is observed to decrease from ~ 900 s at ground to ~ 300 s at 30 km altitude in the case where the lifting gas is hydrogen. Diffusion occurs faster at higher altitude as a result of the lower mass density of the lifting gas.

Appendix B

Convergence study of the finite element code

In the balloon ascent model, Eq. (4) is discretized spatially according to the Finite Element Method. The numerical solution is expressed in terms of a basis of second-order polynomials, which corresponds to a discretization scheme of second order in space. Regarding the time discretization, the first-order Euler backwards scheme is preferred – for stability

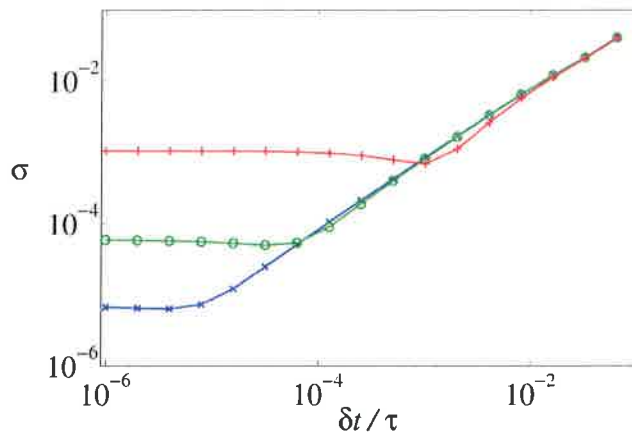


Fig. B1. Variation of σ at $t = 0.1\tau$ as a function of the time step. Three different space discretization intervals are considered: $\delta r = 10^{-2}$ (×); $\delta r = 2 \times 10^{-2}$ (●); and $\delta r = 5 \times 10^{-2}$ (+).

purposes – to the second-order Crank-Nicolson one. The latter introduces oscillations in the numerical solution when used in association with the Finite Element Method.

Convergence of the numerical solution is analyzed here in the simple reference case where the initial temperature inside the balloon is uniform and the temperature at the balloon's surface is constant. Let $T_{b,ana}$ and $T_{b,num}$ respectively denote the analytical and numerical solutions in this case, the expression of $T_{b,ana}$ being derived from Eq. (A2). Convergence is measured in terms of the second moment of the difference $T_{b,ana} - T_{b,num}$,

$$\sigma^2(t) = \frac{3}{(T_a - T_{b,0})^2} \int_0^1 r^2 [T_{b,ana}(r, t) - T_{b,num}(r, t)]^2 dr, \quad (B1)$$

where T_a and $T_{b,0}$ are defined as in Appendix A. The quantity σ corresponds to the numerical error averaged over the balloon volume and normalized by the initial temperature difference between the inside and the outside of the balloon.

Let δr and δt respectively denote the space discretization interval and the time step used by the numerical scheme. Variation of σ at a fixed time as a function of δt is shown in Fig. B1 for three different values of δr . It is observed that the numerical error scales linearly with the time step and saturates for small values of δt . The error does not depend on δr for large time steps, contrary to the saturation value. This implies that a finer spatial discretization is valuable only if conjugated with a finer time resolution. In practice, a time step of $10^{-3}\tau$ is chosen in the balloon ascent model, as it is observed to result in relatively short computational times (not shown) while leading to an acceptable mean error of 0.1 % compared to the analytical solution. This implies that a space discretization as large as 5×10^{-2} can be used, as a finer choice of δr would not improve the precision of the numerical solution (see Fig. B1).

Acknowledgements. We gratefully acknowledge the LUAMI team for its careful work, without which this study would have been much more intricate. We also thank Hendrick Huwald at École Polytechnique Fédérale de Lausanne (EPFL, Lausanne, Switzerland) for fruitful discussions and his revision of our work. This work was in part supported within the COST action ES0904, Atmospheric Water Vapour in the Climate System, funded by the Swiss State Secretariat for Education and Research (SER).

Edited by: A. Stoffelen

References

- Achenbach, E.: Experiments on the flow past spheres at very high Reynolds numbers, *J. Fluid Mech.*, 54, 565–575, 1972.
- Alexander, M., Geller, M., McLandress, C., Polavarapu, S., Preusse, P., Sassi, F., Sato, K., Eckermann, S., Ern, M., Hertzog, A., Kawatani, Y., Pulido, M., Shaw, T. A., Sigmond, M., Vincent, R., and Watanabe, S.: Recent developments in gravity-wave effects in climate models and the global distribution of gravity-wave momentum flux from observations and models, *Q. J. Roy. Meteorol. Soc.*, 136, 1103–1124, doi:10.1002/qj.637, 2010.
- Carlsaw, H. and Jaeger, J.: *Conduction of Heat in Solids*, Clarendon Press, 2nd Edn., 1959.
- Engel, I.: *Trajectory Modelling of Match Balloon Soundings for Cirrus Cloud Characterisation*, Master's thesis, Swiss Federal Institute of Technology Zurich, 2009.
- Fritts, D. and Alexander, M.: Gravity wave dynamics and effects in the middle atmosphere, *Rev. Geophys.*, 41, 1003, doi:10.1029/2001RG000106, 2003.
- Geller, M. A. and Gong, J.: Gravity wave kinetic, potential, and vertical fluctuation energies as indicators of different frequency gravity waves, *J. Geophys. Res.*, 115, D11111, doi:10.1029/2009JD012266, 2010.
- Gong, J. and Geller, M. A.: Vertical fluctuation energy in United States high vertical resolution radiosonde data as an indicator of convective gravity wave sources, *J. Geophys. Res.*, 115, D11110, doi:10.1029/2009JD012265, 2010.
- Govardhan, R. and Williamson, C.: Vortex-induced vibrations of a sphere, *J. Fluid Mech.*, 531, 11–47, doi:10.1017/S0022112005003757, 2005.
- Hamilton, K. and Vincent, R.: High-resolution radiosonde data offer new prospects for research, *EOS Transactions*, 76, 497, doi:10.1029/95EO00308, 1995.
- Hoyle, C., Luo, B., and Peter, T.: The origin of high ice crystal number densities in cirrus clouds, *J. Atmos. Sci.*, 62, 2568–2579, 2005.
- Immler, F.: Report on the LUAMI campaign, Tech. Rep., WMO, available at: http://www.hydrometeoindustry.org/Meetings2008/LUAMI_Lindengerg_Nov2008/LUAMI.v2.pdf, last access: Fall 2008, 2008.
- Lane, T. P., Reeder, M. J. and Guest, F. M.: Convectively generated gravity waves observed from radiosonde data taken during MCTEX, *Q. J. Roy. Meteorol. Soc.*, 129, 1731–1740, doi:10.1256/qj.02.196, 2003.
- Lewis, R., Morgan, K., Thomas, H., and Seetharamu, K.: *The Finite Element Method in Heat Transfer Analysis*, John Wiley & Sons Inc, 1996.

- Loth, E.: Drag of non-spherical solid particles of regular and irregular shape, *Powder Technol.*, 182, 342–353, 2008.
- Mapleson, W.: The drag of spherical rubber balloons, *Q. J. Roy. Meteorol. Soc.*, 80, 449–451, 1954.
- Musso, I., Cardillo, A., Cosentino, O., and Memmo, A.: A balloon trajectory prediction system, *Adv. Space Res.*, 33, 1722–1726, doi:10.1016/j.asr.2003.07.044, 2004.
- Neve, R.: The importance of turbulence macroscale in determining the drag coefficient of spheres, *Int. J. Heat Fluid Fl.*, 7, 28–36, 1986.
- Palumbo, R.: A Simulation Model for Trajectory Forecast, Performance Analysis and Aerospace Mission Planning with High Altitude Zero Pressure Balloons, Ph.D. thesis, Università degli Studi di Napoli “Federico II”, available at: http://www.fedoa.unina.it/1839/1/Palumbo_Ingegneria_Aerospaziale_Navale_e_della_Qualita.pdf, 2007.
- Rex, M., Von Der Gathen, P., Braathen, G., Harris, N., Reimer, E., Beck, A., Alfier, R., Krüger-Carstensen, R., Chipperfield, M., De Backer, H., Balis, D., O'Connor, F., Dier, H., Dorokhov, V., Fast, H., Gamma, A., Gil, M., Kyrö, E., Litynska, Z., Mikkelsen, I. S., Molyneux, M., Murphy, G., Reid, S. J., Rummukainen, M., and Zerefos, C.: Chemical ozone loss in the arctic winter 1994/95 as determined by the match technique, *J. Atmos. Chem.*, 32, 35–59, 1999.
- Salsa, S.: *Partial Differential Equations in Action: From Modelling to Theory*, Springer, 2008.
- Shutts, G., Kitchen, M., and Hoare, P.: A large amplitude gravity wave in the lower stratosphere detected by radiosonde, *Q. J. Roy. Meteorol. Soc.*, 114, 579–594, doi:10.1002/qj.49711448103, 1988.
- Son, K., Choi, J., Jeon, W., and Choi, H.: Effect of free-stream turbulence on the flow over a sphere, *Phys. Fluids*, 22, 045101, doi:10.1063/1.3371804, 2010.
- Vargaftik, N., Flippov, Lev, P., and Tarzimanov, Amin, A.: *Handbook of Thermal Conductivity of Liquids and Gases*, CRC Press, ISBN: 0-8493-9345-0, 1994.
- Veldhuis, C., Biesheuvel, A., and Lohse, D.: Freely rising light solid spheres, *Int. J. Multiphas. Flow*, 35, 312–322, doi:10.1016/j.ijmultiphaseflow.2009.01.005, 2009.
- Vennard, J. K. and Street, R. L.: *Elementary Fluid Mechanics*, Wiley, 5th Edn., 1976.
- Wang, J., Bian, Jianchun, Brown, William O., Cole, Harold, Grubišić, Vanda, Young, Kate: Vertical air motion from T-REX radiosonde and dropsonde data, *J. Atmos. Ocean. Tech.*, 26, 928–942, 2009.
- Yajima, N., Imamura, T., Izutsu, N., and Abe, T.: *Scientific Ballooning*, Springer, Berlin; ISBN: 978-0-387-09725-1, 2009.
- Zink, F. and Vincent, R.: Wavelet analysis of stratospheric gravity wave packets over Macquarie Island – 2. Intermittency and mean-flow accelerations, *J. Geophys. Res.*, 106, 10289–10297, 2001.